

Geochemistry, Geophysics, Geosystems

RESEARCH ARTICLE

10.1029/2019GC008425

Key Points:

- Cenozoic intermediate magmas erupted above the stagnant Pacific slab were hot and volatile-poor
- The magmas are interpreted to represent largely unfractionated, asthenosphere-derived melts
- Sources are volatile-poor, oxidized, and eclogite-rich, characterizing negative seismic velocity anomalies in the mantle

Supporting Information:

- Supporting Information S1

Correspondence to:

S. Erdmann,
saskia.erdmann@cnsr-orleans.fr

Citation:




Erdmann, S., Chen, L.-H., Liu, J.-Q., Xue, X.-Q., & Wang, X.-J. (2019). Hot, volatile-poor, and oxidized magmatism above the stagnant Pacific plate in Eastern China in the Cenozoic. *Geochemistry, Geophysics, Geosystems*, 20. <https://doi.org/10.1029/2019GC008425>

Received 2 MAY 2019

Accepted 22 SEP 2019

Accepted article online 18 OCT 2019

Hot, volatile-poor, and oxidized magmatism above the stagnant Pacific plate in Eastern China in the Cenozoic

S. Erdmann^{1,2} , L.-H. Chen¹ , J.-Q. Liu^{1,3}, X.-Q. Xue¹, and X.-J. Wang¹ 

¹State Key Laboratory for Mineral Deposits Research, School of Earth Sciences and Engineering, Nanjing University, Nanjing, China, ²Université d'Orléans-CNRS/INSU-ISTO-BRGM, UMR 7327, Orléans, France, ³College of Oceanography, Hohai University, Nanjing, China

Abstract Eastern China has experienced widespread and voluminous, basaltic to andesitic intraplate magmatism in the Cenozoic. Seismic tomography and kinematic reconstructions show that magmas have erupted above the stagnant Pacific plate, which currently extends within the mantle transition zone for >1500 km beyond the active arc. Seismic studies also show in intriguing detail that low-velocity wave anomalies reach from the mantle transition zone or below to major volcanic centers, suggesting an intimate relation between the magmatism and components derived from the mantle-transition zone and possibly from deeper levels. Here, we provide new petrological, mineral chemical, and whole-rock geochemical data showing that Cenozoic basaltic andesitic and andesitic magmas that have erupted above the present-day edge of the subducted Pacific plate are largely unfractionated, $\geq 1130\text{--}1160 \pm 15\text{--}50$ °C hot, mantle-derived melts that were volatile-poor (undegassed melt CO₂ and H₂O of $\sim 2400\text{--}3100 \pm 500$ ppm and $\sim 0.5\text{--}0.6 \pm 0.4\text{--}1.1$ wt%), and relatively oxidized ($\sim \text{FMQ}$ to $\sim \text{FMQ} + 1.3 \pm 1.0$). We further infer that the magmas were derived by partial melting of oxidized, H₂O- and CO₂-poor eclogite-rich sources ($\sim \text{FMQ}\text{--}1.0$ to $\sim \text{FMQ}$). We use this to suggest that the low-velocity seismic anomalies below Eastern China largely reflect the presence of oxidized and enriched, hot and not necessarily particularly hydrous mantle domains as common interpretation has suggested. This is crucial information for quantifying material flow above and around the subducted Pacific plate and for constraining residence times of subducted components in Eastern Asia and globally.

1. Introduction

One of the world's most intriguing regions of subduction zone to intraplate magmatism is located in eastern Asia, where large volumes of sodic basaltic, but also potassic basaltic and basaltic andesitic and andesitic magmas have erupted. Seismic tomography reveals that the Pacific plate, subducted along the Japan-Izu-Bonin-Mariana arc, stagnates in the mantle transition zone below Eastern China, Russia, and the Koreas, currently extending for >1,500 km beyond the arc (Figure 1; Fukao et al., 2009; Huang & Zhao, 2006; Zhao, 2004). Low S and P wave velocity anomalies extend from the top of the mantle transition zone, and possibly from the deep mantle, to several of the Cenozoic volcanic centers (e.g., at Changbaishan, Wudalianchi, Halaha; Figure 1a), suggesting a close relation between the mantle transition zone and the wide-spread volcanism (Chen et al., 2017; Huang & Zhao, 2006; Kimura et al., 2018; Tang et al., 2014; Wei et al., 2019; Zhao, 2004). Many geochemical studies have further shown that enriched mantle components play an important role in the formation of the magmas, which are thought to derive from the stagnant Pacific slab and/or from ancient subducted slabs (Kimura et al., 2018; Kuritani et al., 2011, 2019; Tang et al., 2014; Wang et al., 2017; Xu et al., 2018).

The low P and S wave velocity (V_P and V_S) anomalies that are linked to Eastern China's volcanism have been interpreted to delineate hydrous and hot mantle upwelling (Chen et al., 2017; Huang & Zhao, 2006; Wei et al., 2019; Zhao, 2004), as global electromagnetic induction studies indicate that the mantle transition zone is extremely wet with $\sim 0.1\text{--}0.4$ wt% H₂O or more, with volatiles derived from the dehydration of the stagnant Pacific and ancient slabs (Kelbert et al., 2009). Interpreting the record of seismic wave velocity anomalies is, however, far from straightforward. Geophysical studies are unrivalled in providing a detailed spatial image of geosystems including that of magma systems extending from the mantle to the surface, but wave velocity

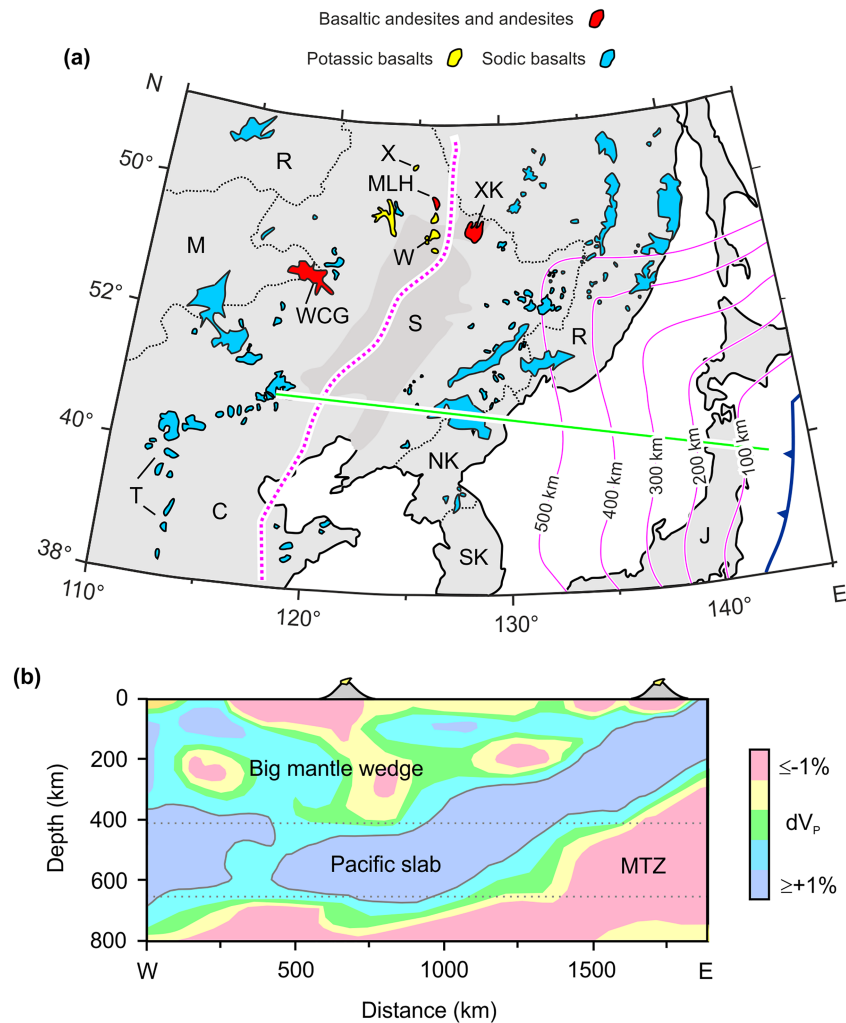


Figure 1. (a) Overview map showing the occurrence of Cenozoic, basaltic to andesitic intraplate magmatism in eastern Asia above the stagnant Pacific plate (re-drawn from maps of Huang & Zhao, 2006; Tang et al., 2014; and Wang et al., 2017). The solid pink lines depict the estimated average depth of the subducted slab. The stippled pink line marks the surface projection of the westernmost, present-day extension of the stagnant Pacific slab. The solid green line highlights the location of the seismic profile schematically shown in (b). MLH=Menluhe; XK=Xunke, WCG=Wuchagou; C=China; NK=North Korea; SK= South Korea; M=Mongolia; R=Russia; S=Songliao Basin; T=Taihang mountains; W=Wudalianchi; X=Xiaogulihe. (b) Profile schematically depicting regional seismic P wave velocity anomalies (dV_P) shown by Chen et al. (2017); sketched after their Fig. 6c. Seismic tomography as sketched in the profile shows the stagnant subducted slab of the Pacific plate with a possible slab break. The stagnant Pacific plate is characterized by high seismic velocities anomalies ($dV_P \geq +1\%$), while the big mantle wedge above shows several low-velocity seismic anomalies ($dV_P \leq -1\%$; see also Fukao et al., 2009; Huang & Zhao, 2006; Wei et al., 2019). Note that the near-surface low- V_P anomalies image crustal lithologies. MTZ= mantle transition zone.

variations may have various origins, including variations in temperature, composition, oxygen fugacity, the absence/presence of partial melt and fluids, and/or high crack densities (Behn & Kelemen, 2003; Cline et al., 2018; Karato, 2011). Variable hydroxyl content (variable “H₂O” in minerals) has, in contrast to common interpretation, a very minor effect on wave speeds of normal upper mantle rocks (Cline et al., 2018; Karato, 2011), and the low-velocity anomalies in the mantle below Eastern China are thus no compelling evidence for wet mantle upwelling.

To rigorously and robustly interpret the seismic wave velocities and thus mantle components and partial melting conditions beneath Eastern Asia, it is imperative to better link geophysical, geochemical, and petrological observations. Here, we present (1) petrological constraints on melt H₂O and CO₂ contents, temperatures, and oxygen fugacities of Cenozoic basaltic andesitic and andesitic magmas that have erupted above the

present-day edge of the stagnant Pacific plate (Figure 1a); and (2) geochemical constraints on the source lithologies and source volatile contents of the intermediate magmas, which we use to interpret observed seismic anomalies. We have targeted the basaltic andesitic and andesitic systems because they are inferred to have erupted largely unfractionated and largely uncontaminated mantle-derived melts (Lim et al., 2017), yet have mineral assemblages and melt inclusions that permit robust constraints on various intensive system parameters.

2. Background and Geological Setting

Seismic tomography shows that the Pacific plate, which is characterized by positive wave anomalies (dV_S and dV_P of up to +6% and +4%), stagnates at a depth of ~400–700 km below Eastern China, Russia, North Korea and South Korea, currently extending to ~120–130 °E (Figures 1a and 1b; Chen et al., 2017; Huang & Zhao, 2006; Tang et al., 2014). When exactly the stagnant Pacific slab has developed is a point of debate (e.g., Kimura et al., 2018; X. Liu et al., 2017; Xu et al., 2018), but kinematic reconstructions suggest that the slab has ponded in the mantle transition zone for at least 25 Ma, following subduction, flat slab stagnation, and slab break-off of the Izanagi plate at >35 Ma (Jolivet et al., 2018; Kimura et al., 2018). The flat slab of the Pacific plate has grown in extent since ≥ 25 Ma, while its edge has remained close to the western border of present-day Mongolia (Jolivet et al., 2018; Kimura et al., 2018), where Eastern Asia's lithosphere has moved essentially on a N-S trajectory for at least ~40 Ma (Jolivet et al., 2018).

The large-scale geodynamic situation—that is the presence of the stagnant Pacific slab in the mantle transition zone and a big mantle wedge beneath eastern China – has thus remained largely unchanged for >10–25 Ma. Upwelling from the mantle transition zone and lower upper mantle or the deep mantle has also been proposed to have been active for >15 Ma, and thus for the entire younger Cenozoic (i.e., Quaternary and Neogene; Kimura et al., 2018; Kuritani et al., 2011, 2019; Tang et al., 2014; Wang et al., 2017; Xu et al., 2018). The present-day mantle above the stagnant plate, the so-called big mantle wedge – and also the upper mantle beyond it to the west and the lower mantle – shows large-scale dV_S and dV_P anomalies of mostly $\leq \pm 3\%$ and $\pm 2\%$ (Figure 1b; Chen et al., 2017; Huang & Zhao, 2006; Kimura et al., 2018; Tang et al., 2014; Wei et al., 2019). The upper mantle seismic anomalies compare in intensity to those of, for example, the Yellowstone mantle plume ($dV_S = -4$ to +2%, $dV_P = -2$ to +1%; Waite et al., 2006), but they are small compared to velocity variations in volcanic arc systems (with velocity anomalies of commonly up to $\pm 10\%$; Widiyantoro et al., 2018).

Several of the low-velocity anomalies beneath Eastern China unquestionably extend from the top of the mantle transition zone to the surface, while it remains debated if they also locally connect through slab gaps to the lower mantle (Chen et al., 2017; Tang et al., 2014; Wei et al., 2019), or if they connect to a deep mantle plume (i.e., the Datong mantle plume; Kimura et al., 2018). The large scale of the seismic anomalies in the upper mantle (Figure 1) and vertical mantle flow velocities (≤ 4 cm/year; Cheng et al., 2006) highlight that the presently observed anomalies must have developed >10 Ma ago. The location and the geometry of the anomalies has likely varied through time, but at least some are long-lived, for example, the one that has fed magma to the Wudalianchi, Erkeshan, and Keluo volcanic field (~9.6 Ma to 1721 AD), which is spatio-temporally associated with the magma systems that we have studied (Figure 1a).

The Cenozoic magmatism above the big mantle wedge, with over 500 volcanic centers, is predominantly sodic basaltic, where melts are inferred to have formed in the asthenosphere from depleted sources with minor contributions from enriched components (Figure 1a; Chen et al., 2007; Wang et al., 2017; Xu et al., 2018; Zou et al., 2008). The largest volcanic centers occur along lithosphere-scale fault systems and above parts of the subducted Pacific plate where breaks or other zones of weakness are present, which are inferred to have promoted upwelling from the mantle transition zone and possibly permitted upwelling from the lower mantle through slab breaks (Faccenna et al., 2010; Tang et al., 2014). Potassic basaltic, basaltic andesitic and andesitic magmatism, in contrast, is abundant above or close to the present-day edge of the stagnant Pacific plate and above some of the major low- V_P , low V_S anomalies (Figure 1a; Fan & Hooper, 1991; Ho et al., 2013; Kuritani et al., 2011, 2013; Lim et al., 2017; Liu et al., 1994; Wang et al., 2017; Xu et al., 2018). Most studies conclude that the potassic basalts derive from enriched mantle (EM1-type) which contains subducted sedimentary eclogite, where melts formed during upwelling in the asthenosphere and subsequently reacted with the lithosphere (Kuritani et al., 2013; Liu et al., 2016, J.-Q. Liu et al., 2017; Wang et al., 2017; Xu et al., 2018). The basaltic andesitic and andesitic Wuchagou magmas are equally interpreted to have been derived

from partial melting of eclogite (close to enriched EM1-type composition) in the asthenosphere and are inferred to have been affected by limited melt-peridotite reaction (Lim et al., 2017), while a mixed lithosphere-crust origin has also been invoked (Ho et al., 2013). Most or some of the enriched source components are thought to derive from the Pacific plate, while others have been subducted >1–2 Ga ago (Kuritani et al., 2011; Wang et al., 2017).

Eruption temperatures of the potassic basalts are inferred to have been ~1150–1300 °C, and thus high (Kuritani et al., 2013; Zhang et al., 2016), while those of the basaltic andesitic and andesitic lavas are unknown. Mantle potential temperatures have been estimated to be ~1290 to ~1340 °C below Wudalianchi, i.e. close to our study area (Kuritani et al., 2013; Kimura et al., 2018; Figure 1a). Melt H₂O contents appear to be moderately low (~0.3–1.4 wt%) to moderately high (up to ~4 wt%) for basalts erupted above the near-edge region of the Pacific plate and for basalts erupted above the big mantle wedge, respectively (Chen, Xia, & Ingrin, 2015; Chen, Xia, Ingrin, Jia, et al., 2015; Kuritani et al., 2013; Liu, Xia, Deloule, Chen, et al., 2015; Liu, Xia, Deloule, Ingrin, et al., 2015; Xu et al., 2018), but melt H₂O contents of the erupted basaltic andesites and andesites remain unconstrained. The CO₂ contents of the magma systems and the level at which volatile saturation occurs have not been investigated yet. The redox state of the magma systems also remains unconstrained, while moderately reducing conditions (~FMQ) have been assumed in thermodynamic model calculations (Kuritani et al., 2013).

3. Samples, Methods, and Data

The largest volumes of the Cenozoic basaltic andesitic and andesitic magmas have erupted at the Menluhe, Xunke, and Wuchagou volcanic centers, which we have sampled (Figure 1a). The Menluhe and the Xunke lavas are ~1.3–1.0 Ma and <1.0 Ma old (J. Q. Liu et al., 2017; Zhao et al., 2014), while the Wuchagou andesites have ages of ~8.0 to 10.5 Ma (Ho et al., 2013). The three studied volcanic centers may have had a different location relative to the edge of the stagnant slab than at present (Figure 1a) when they were active, but we presume that the difference was minor, because the edge of the stagnant slab appears to have remained in approximately the same location beneath Eastern Asia, while Eastern Asia's lithosphere has moved in ~N-S direction (Jolivet et al., 2018). We also highlight that current seismic anomalies and those that existed ~1 or 10 Ma ago may have unquestionably differed in size, shape, and location, but we argue that insights gained from the three investigated systems can be used to interpret current mantle composition, conditions, and seismic anomalies.

We have characterized whole-rock major-element compositions for 23 samples from the Menluhe volcanic center and report those of the Xunke and the Wuchagou volcanic centers, which were previously determined by our group (Lim et al., 2017; J. Q. Liu et al., 2017) to infer possible source lithologies of the magmas. All whole-rock compositions were determined at the State Key Laboratory for Mineral Deposits Research, Nanjing University, using a Thermo Scientific ARL 9900 X-ray fluorescence spectrometer (XRF). According to the measured values of rock reference material (BHVO-2), the uncertainties (relative standard deviation) are less than 1% for Si, Al, Fe, Mg, Ca, Na and Ti, and less than 3% for Mn and K. From the >70 samples that we have geochemically characterized and studied in thin section, we have chosen a subset of 15 samples (five from each location) to quantify phase assemblages and mineral compositions to constrain temperature, pressure, *f*O₂, and melt H₂O during partial crystallization. The Menluhe mineral compositions and all glass inclusion compositions were quantified using a Cameca SX Five microprobe at the Institut des Sciences de la Terre d'Orléans (ISTO), France, at the shared CNRS-UO-BRGM facility. The Xunke and the Wuchagou mineral compositions were determined using a JEOL JXA-8100 Superprobe at Nanjing University, China, at the State Key Laboratory for Mineral Deposits Research. Selected crystals from the Xunke samples were analyzed at both laboratories, which gave equivalent results within analytical uncertainty. Operating conditions were set to 15 keV and 6 nA (at ISTO) and to 15 keV and 10 nA (at Nanjing University) with peak and background counting times of 10–20 s. All minerals were analyzed with a focused beam; the glass inclusions were analyzed with a defocused, 5 μm beam. Alkali migration in glasses under the electron beam was monitored relative to glass standards of Scaillet and Evans (1999), but was insignificant for the characterization of the anhydrous glass inclusions.

In addition, laser ablation inductively coupled mass spectrometry (LA-ICP-MS) was used to determine element concentrations including those of Ca, V, Sc, and Y for selected olivine crystals cores and their host

matrix. The analyses were performed at the ISTO-CNRS facility in Orléans, France, using a RESOLUTION-SE laser ablation system with a Laurin Technic samples cell coupled to an Agilent 8900 QQQ mass spectrometer. Point and line-scan analyses (olivine and matrix, respectively) were performed at a fluence of 5 J/cm² and at a repetition rate of 8 Hz. Background signals were acquired for 30 s preceding each analysis. Point analyses (olivine) were performed for 40 s with a 64- μ m beam diameter. Line-scan analyses (matrix) were performed for 100 s at a scan speed of 10 μ m/s and with a 100 μ m beam diameter. BCR-2G (USGS) and GOR132 (MPI-DING) glasses were used as external standard and as quality controls. SiO₂ was used as the internal standard. Ca, Y, V, Sc, and Si were analyzed as ⁴³Ca, ⁸⁹Y, ⁵¹V, ⁴⁵Sc, and ²⁹Si. Raw data were processed off-line using Glitter, where quality control analyses on GOR132 glass showed Ca, Y, V, and Sc values deviating by -0.4%, +0.2%, -2.2%, and -13.0% from published values (GeoRem preferred values with Y=36.5 ppm, V=214 ppm, and Sc=12.9 ppm). For olivine, we have integrated signals over 30–40 s of the ablation signal. Our analyses of the matrix, which is composed of coarse-grained clinopyroxene, \pm olivine, plagioclase, magnetite, ilmenite, and devitrified glass, yielded predictably heterogeneous signals. These were averaged for each line scan and then averaged for 3 to 5 line scans per sample to estimate a representative matrix composition.

Mineral abbreviations used in text and figures follow those of Whitney and Evans (2010). Reported mineral end-member compositions are percentage forsterite {Fo=[Mg/(Mg+Fe_{tot})]*100} for olivine, enstatite {En=[Mg/(Mg+Fe_{tot}+Ca)]*100} and wollastonite {Wo=[Ca/(Ca+Mg+Fe_{tot})]*100} for orthopyroxene and clinopyroxene, and anorthite {An=[Ca/(Ca+Na+K)]*100} and orthoclase {Or=[K/(K+Ca+Na)]*100} for plagioclase. Normal zoning refers to rim ward decreasing Mg in olivine and in the pyroxenes and decreasing Ca in plagioclase. All Fe in olivine and in orthopyroxene was assumed to be Fe²⁺. Fe²⁺/Fe³⁺ for melts was calculated using equation 7 of Kress and Carmichael (1991); Fe²⁺/Fe³⁺ for spinel was calculated assuming charge balance. To estimate the conditions of partial crystallization, we have paired mineral core compositions with estimated equilibrium melt compositions, which were calculated using whole-rock compositions minus the bulk of phenocryst compositions. We have used this approach and present the calculated values as our preferred estimates because the phenocrysts have unzoned core compositions and normally zoned rims that make up a minor proportion (<5–10% of the crystals). Calculated partition coefficients (Table S2 in the supporting information) are close to equilibrium values, validating our approach. To nevertheless assess the uncertainty that may have been introduced, we have also calculated crystallization conditions and partition coefficients using mineral core and bulk-rock compositions, which provides extreme estimates. All values are reported in Supporting Information Table S2, while the main text provides our preferred values. The mineral core and estimated equilibrium melt compositions were used in combination with (1) the orthopyroxene-liquid barometer of Putirka (2008); equation 29a with a standard error of $\sim\pm 260$ MPa; (2) the orthopyroxene-melt, olivine-melt, and melt-only thermometers of Putirka (2008; equations 15, 22, 28a with standard errors of $\sim\pm 50$ °C) and the olivine-melt-Sc/Y thermometer of Mallmann and O'Neill (2013; with a standard error of $\sim\pm 15$ °C); (3) the olivine-spinel oxygenbarometer of Nikolaev et al. (2016) and the olivine-melt-V oxybarometer of Mallmann et al. (2013); with standard errors of $\sim\pm 0.3$ and $\sim\pm 1$ log units; and (4) the plagioclase-liquid hygrometers of Putirka (2008; equation 25b) and Waters and Lange (2015) with standard errors of $\sim\pm 1.1$ and $\sim\pm 0.4$ wt% H₂O, respectively. In addition, we have performed limited phase-equilibrium and fractionation modeling using the PELE software (Boudreau, 1999). Details on all methods and their uncertainties are provided in the Supporting Information files (Texts S1 to S5).

All employed calibrations except for the two oxybarometers and the Sc/Y olivine thermometer are applicable to the intermediate compositions of our systems. The latter, in contrast, have been calibrated for ultramafic to mafic compositions, and we therefore have to assess if they can be assumed to derive realistic estimates of crystallization conditions for our basaltic andesitic and andesitic systems. We have tested the Nikolaev et al. (2016) olivine-spinel oxybarometer on olivine and spinel compositions produced in andesite crystallization experiments of Grove et al. (2003) and Krawczynski et al. (2012), which were buffered at FMQ and NNO. Calculated conditions are FMQ-0.1 (for FMQ) and NNO+0.2 (for NNO) and they thus closely concur with the imposed experimental conditions, justifying the application of the Nikolaev et al. (2016) oxybarometer to our systems. V and Sc/Y olivine-melt partitioning predominantly depend on f O₂ and temperature, but also on olivine and melt composition. The Fo content of our olivine crystal cores (Fo=74–82) is within the range (Fo=60–100) of the Mallmann et al. (2013) calibration database, but our melt compositions have lower CaO

Table 1
Calculated Intensive Parameters (Preferred Values) and Partition Coefficients for Phenocryst Core Compositions

Parameter	Method	Menluhe	Xunke	Wuchagou
P (MPa)	(1) Opx-L	421–590, $\emptyset 517 \pm 260$ –500	597–665, $\emptyset 637 \pm 260$ –500	137–494, $\emptyset 331 \pm 260$ –500
	(2) L-CO ₂	360–580, $\emptyset 510 \pm 50$ –100	360–490, $\emptyset 430 \pm 50$ –100	300–510, $\emptyset 420 \pm 50$ –100
T (°C)	(3) Ol-L (Sc/Y)	1,093–1,174, $\emptyset 1,136 \pm 15$ –50	1,127–1,159, $\emptyset 1,145 \pm 15$ –50	1,161–1,178, $\emptyset 1,170 \pm 15$ –50
	(4) Opx-L	1,137–1,162, $\emptyset 1,149 \pm 50$ –90	1,155–1,166, $\emptyset 1,163 \pm 50$ –90	1,140–1,179, $\emptyset 1,156 \pm 50$ –90
	(5) Ol-L	1,101–1,126, $\emptyset 1,115 \pm 50$ –90	1,086–1,146, $\emptyset 1,116 \pm 50$ –90	1,140–1,165, $\emptyset 1,152 \pm 50$ –90
	(6) L	1,121–1,135, $\emptyset 1,128 \pm 50$ –90	1,102–1,142, $\emptyset 1,123 \pm 50$ –90	1,138–1,158, $\emptyset 1,148 \pm 50$ –90
	Av.	1,132	1,137	1,157
H ₂ O _m (wt%)	(7) Pl-L	0.1–0.4, $\emptyset 0.3 \pm 0.4$ –1.1	0.5–0.6, $\emptyset 0.6 \pm 0.4$ –1.1	–0.1–0.3, $\emptyset 0.1 \pm 0.4$ –1.1
	(8) Pl-L	0.4–0.8, $\emptyset 0.6 \pm 1.1$ –2.2	0.4–0.8, $\emptyset 0.5 \pm 1.1$ –2.2	0.6–1.4, $\emptyset 1.0 \pm 1.1$ –2.2
	Av.	0.5	0.6	0.6
<i>f</i> O ₂ (FMQ+log)	(9) Ol-Spl	0.9–1.0, $\emptyset 0.9 \pm 1.0$ –1.3	0.4–0.9, $\emptyset 0.7 \pm 1.0$ –1.3	–0.4–0.5, $\emptyset 0.0 \pm 1.0$ –1.3
	(10) Ol-L (V)	1.0–2.2, $\emptyset 1.7 \pm 0.3$ –1.1	0.6–1.4, $\emptyset 1.1 \pm 0.3$ –1.1	–0.1–0.3, $\emptyset 0.0 \pm 1.0$ –1.3
	Av.	1.3	0.9	0.0
K _D	Pl-L (Ca/Na)	0.21–0.33, $\emptyset 0.25$	0.16–0.26, $\emptyset 0.20$	0.18–0.31, $\emptyset 0.25$
	Ol-L (Fe/Mg)	0.23–0.33, $\emptyset 0.27$	0.27–0.36, $\emptyset 0.30$	0.27–0.36, $\emptyset 0.30$
	Opx-L (Fe/Mg)	0.22–0.26, $\emptyset 0.24$	0.25–0.28, $\emptyset 0.26$	0.25–0.34, $\emptyset 0.30$
	Spl-Ol (Fe/Mg)	2.6–3.0, $\emptyset 2.8$	1.7–2.3, $\emptyset 2.0$	1.9–2.9, $\emptyset 2.4$

Note. P: pressure; T: crystallization temperature; H₂O_m: melt H₂O content; *f*O₂: oxygen fugacity; K_D: partition coefficient; L: estimated equilibrium melt composition. Calibrations used are those of (1, 4–6, 8) Putirka (2008); (2) Papale et al. (2006); (3, 10) Mallmann et al. (2013); (7) Waters and Lange (2015); and (9) Nikolaev et al. (2016). Details on the methods and our complete datasets are reported in are reported in Texts S1 to S5 and Table S2. Errors reported here are standard errors (e.g., ± 260 MPa) and estimated maximum errors (e.g., ± 500 MPa). Values for spinel-olivine compositional pairs that are considered to have approached equilibrium.

+Na₂O+K₂O and higher SiO₂+Al₂O₃ contents than melt compositions considered in the calibration (Figure S1). The effect of increasing contents of network forming and decreasing contents of network modifying cations, which is considered in the Mallmann and O'Neill (2013) calibrations, is to increase V partitioning and to decrease Sc/Y partitioning in olivine, but it is uncertain if/how far beyond the calibration range the effect is adequately captured. We are not aware of appropriate experimental data for testing the relation, and we therefore later assess the results relative to those calculated using the thermometers of Putirka (2008) and the oxybarometer of Nikolaev et al. (2016).

Crystallization temperatures, oxygen fugacity and melt H₂O contents were iteratively determined using the nine calibrations (Tables 1 and S2). As input parameters, we have used average calculated temperatures, melt H₂O contents, and *f*O₂ in combination with pressure estimated from melt inclusion volatiles (determined as outlined below). We stress that all employed estimates have relatively low standard errors as indicated above, except for the orthopyroxene barometric results, which we have not used for the iterative calculations. Errors on the various estimates, however, may also propagate. Considering standard errors for the input parameters (i.e., ± 50 –100 MPa, ± 50 °C, ± 0.7 –1.1 wt% melt H₂O, ± 0.3 –1.1 log units *f*O₂), we infer maximum errors of (1) $\sim \pm 500$ MPa for the orthopyroxene-melt pressure estimates (relating to uncertainties in temperature and melt H₂O estimates); (2) $\sim \pm 90$ °C for the various thermometric estimates (relating mostly to uncertainties in pressure and melt H₂O estimates); (3) $\sim \pm 1.2$ and $\sim \pm 2.2$ wt% melt H₂O for the Waters and Lange (2015) and the Putirka (2008) hygrometric estimates (mostly relating to uncertainty in temperature estimates); and (4) $\sim \pm 1.0$ and $\sim \pm 1.3$ log units for the *f*O₂ estimates using the Mallmann et al. (2013) and Nikolaev et al. (2016) oxybarometers, respectively (relating to uncertainties in pressure and temperature and olivine and melt compositions). Using the calculated data, we later discuss the likely uncertainties, that is, whether they are likely within standard or maximum errors. We further highlight that the calculated temperatures may be slight underestimates (by <30 °C), and that the calculated melt H₂O contents and *f*O₂ may be slight overestimates (by <0.6 wt% and by <0.4 log units, respectively), resulting from our approach using mineral core compositions and groundmass composition as equilibrium pairs in our calculations (see preferred and extreme values in Table S2 and later discussion in the text).

Melt inclusion textures and melt inclusion vapor bubble compositions were further quantified for two samples from each volcanic center to assess volatile saturation and to determine entrapment melt CO₂ content. The 2-D and 3-D volumes of melt inclusions and their vapor bubbles in phenocrysts were determined using transmitted light microphotographs and the CSDslice spreadsheet of Morgan and Jerram (2006). Uncertainties relate to the precision of the measurements and to estimated 3-D shapes. From repeat measurements, errors are estimated to be ~25% for bubble diameters of ~5 μm, but <5% for bubble diameters of >25 μm. Measurement errors also decrease from small to large melt inclusions, but the irregularity of melt inclusions increases with size, which we could not quantify. We therefore report an average estimated error of 25% for bubble and melt inclusion volumes, which is an overestimate for large bubble volumes. Following our textural analysis, the volatile content of the bubbles in the melt inclusions was characterized using a Renishaw in Via micro Raman spectrometer at the Institut des Sciences de la Terre d'Orléans, France. The analyses were performed using an Argon ion laser operated at a wavelength of 514 nm. Spectra were collected with a 1,800 l/mm grating, at laser output powers of 10–100%, and in confocal mode using a 100x Olympus objective, calibrated against an Si standard. Spectra were first collected between 150 and 4,000 cm⁻¹ in single 60-s scans to test for the presence of volatile species in addition to CO₂. To quantify CO₂ densities, we have then collected spectra between 1,000 and 1,600 cm⁻¹ in three to five 60-s scans. All data were recorded using the Wire3.4 software and processed using Fityk (Wojdyr, 2010). The distance between two CO₂ Raman peaks, the Fermi diad splitting (Δ in cm⁻¹), was used to determine CO₂ vapor densities using the equation of Kawakami et al. (2003; details in Text S6). Entrapment melt CO₂ contents were then calculated for original melt inclusion volumes and melt bulk densities of ~2.60–2.65 g/cm³. Uncertainties in the determined CO₂ densities relate to Raman analytical errors and to peak fitting uncertainties; from repeat analyses, we estimate errors of ~25% and ~10% for the low- and the high-density CO₂ data, respectively. The inferred entrapment melt CO₂ contents have uncertainties relating to the CO₂ densities, the inferred melt inclusion volumes, and the inferred melt inclusion densities. We acknowledge that estimates for individual inclusions may have errors of up to 50%, but the errors are likely random and we therefore suggest that the estimates are likely within 1 σ of the averages (~±500 ppm). In addition to the orthopyroxene-melt compositions, we use the estimated melt CO₂ and H₂O contents and the model of Papale et al. (2006) to infer entrapment and partial crystallization pressures (details in Text S7).

4. Results

4.1. Whole-Rock Major-Element Compositions

Lavas from the Menluhe, Xunke, and Wuchagou volcanic centers show limited major- and minor-element variation, but lavas erupted at each of the volcanic centers differ in composition (Figure 2 and Table S1). The basaltic andesites and andesites are rich in SiO₂ yet poor in TiO₂, MgO, K₂O, and P₂O₅ compared to possible fractionates of sodic and potassic basalts (e.g., Halaha and Nuominhe basalts; Figure 2) that have erupted in spatiotemporal association. The Menluhe samples have the overall lowest SiO₂, and Fe₂O₃ contents (Figure 2c), intermediate MgO content (Figure 2d), yet the highest K₂O and P₂O₅ contents (Figures 2h and 2i) of the three volcanic centers. The Xunke samples have compositions that closely compare to the lavas of the Menluhe volcanic center, yet a larger compositional range, extending to overall higher SiO₂ and Fe₂O₃ (Figure 2c) and lower MgO, K₂O, and P₂O₅ (Figures 2d, 2h, and 2i). The Wuchagou samples have the highest SiO₂ and MgO contents (Figure 2d), but the lowest TiO₂, K₂O, and P₂O₅ contents (Figures 2a, 2h, and 2i). TiO₂/SiO₂, Fe₂O₃/SiO₂, MnO/SiO₂, K₂O/SiO₂, and P₂O₅/SiO₂ of lavas erupted at the three volcanic centers could delineate fractionation, as they define kinked but continuous trends (Figures 2a, 2c, 2e, 2h, and 2i). However, Al₂O₃/SiO₂, MgO/SiO₂, CaO/SiO₂, and Na₂O/SiO₂ compositions show characteristic differences for the Menluhe and Xunke samples, on one hand, and for the Wuchagou samples, on the other hand (Figures 2b, 2d, 2f, and 2g).

4.2. Phase Assemblages and Compositions

The Menluhe, Xunke, and Wuchagou lavas are aphyric with ≤10 vol% phenocrysts and rare xenocrysts (≤1 vol%; e.g., resorbed, irregular-subround quartz and/or sieve-textured subround to subhedral plagioclase). The groundmass of the samples is largely crystallized, comprising ±olivine, clinopyroxene, plagioclase, magnetite, ilmenite, and variable amounts of devitrified glass (Figure 3). The phenocrysts show skeletal and

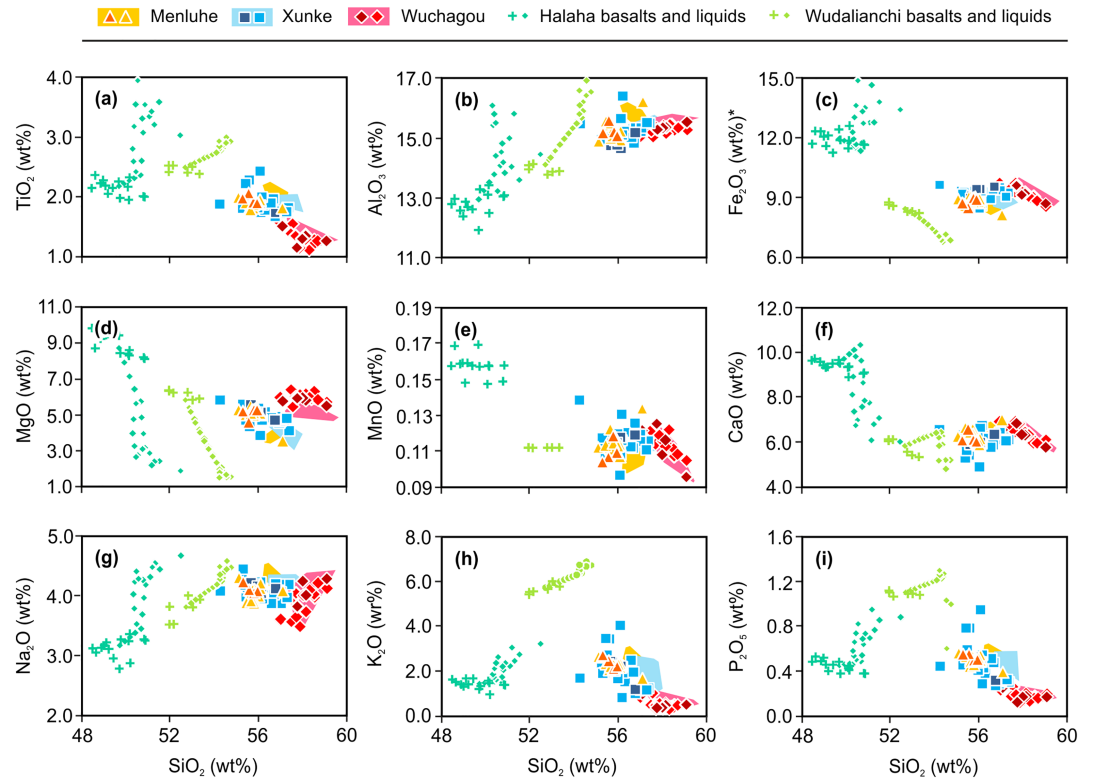


Figure 2. Whole-rock compositions of the Menluhe, Xunke, and Wuchagou lavas (colored symbols) and melt compositions (colored fields) estimated to have been in equilibrium with phenocryst cores (calculated as whole-rock composition minus the bulk of phenocryst compositions). The dark yellow, dark blue, and dark red symbols highlight samples (five for each volcanic center) for which we have determined mineral compositions and estimated the equilibrium melt compositions. The Wuchagou whole-rock compositions are from Lim et al. (2017); the Xunke whole-rock compositions are from J. Q. Liu et al. (2017); the Menluhe whole-rock compositions are our new data. Whole-rock compositions of sodic basalts (Halaha, dark green crosses; data from Ho et al., 2013) and potassic basalts (Wudalinachi, light green crosses; data from Kuritani et al., 2011) and their modeled liquid lines of descent (green diamonds) shown for comparison. Fractionation of the basalts was calculated using the PELE software (Boudreau, 1999), where we modeled cooling from 1250 to 1050 °C, at 200–400 MPa, at FMQ to FMQ+1, and for initial melt H₂O contents of 0.5 to 1.0 wt%. *Fe is shown as Fe₂O₃; all oxides are normalized to 100 wt%.

ehedral-subhedral or anhedral morphologies (Figure 3). The Menluhe and the Xunke lavas have olivine (~2–4 vol%), ±orthopyroxene (~0–1 vol%), ±clinopyroxene (~0–2 vol%), and ±plagioclase (~1–2 vol%) phenocrysts, where orthopyroxene is marginally resorbed and replaced by clinopyroxene (Figure 3b). The comparatively evolved Wuchagou lavas have orthopyroxene (~1–3 vol%), plagioclase (~1–3 vol%) and ±olivine phenocrysts, where orthopyroxene and olivine margins are partially replaced by clinopyroxene.

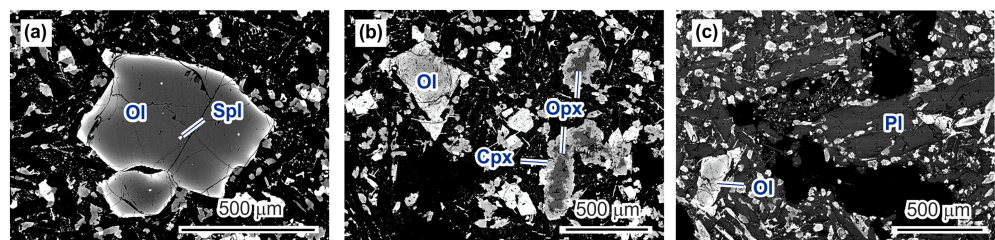


Figure 3. Backscattered electron images of (a) olivine with spinel inclusions (example from Menluhe), (b) olivine and orthopyroxene (example from Xunke), and (c) plagioclase and olivine phenocrysts (example from Wuchagou) surrounded by coarse-grained matrix minerals. Orthopyroxene in (b) is rimmed by and partly replaced by low-Mg clinopyroxene ($X_{Mg} < 80$ to ~65). Crystals have unzoned cores and normally zoned rims, which make up <5–10% of the phenocryst mass.

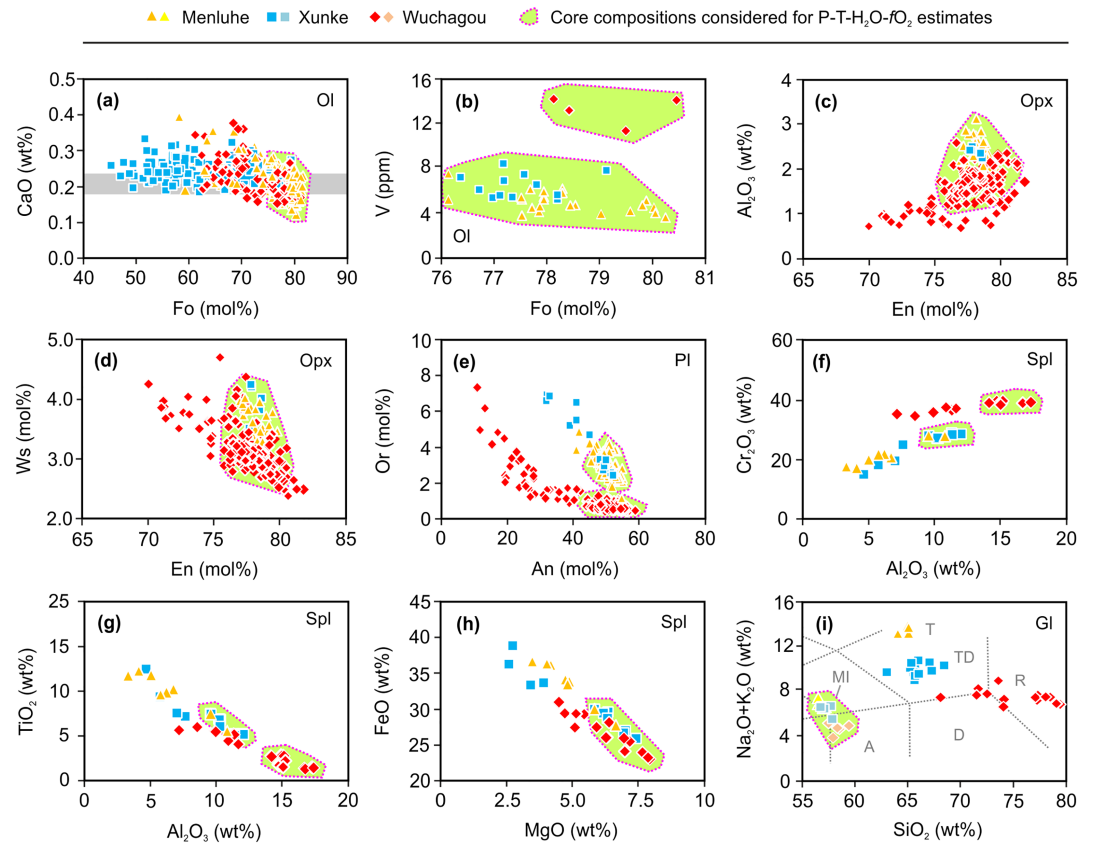


Figure 4. Composition of (a–e) phenocryst cores and rims, (f–h) spinel inclusions, (i) melt inclusions and their residual glasses. Phenocryst core compositions, which we have used for our estimates of crystallization pressure, temperature, melt H_2O , and fO_2 , are highlighted. Rim compositions account for all other data. The mineral and glass compositions closely compare for samples from the Menluhe, Xunke, and Wuchagou volcanic centers, but nevertheless show characteristic differences (e.g., in V for olivine; Al_2O_3 and Ws for orthopyroxene; Or for plagioclase; Al_2O_3 , Cr_2O_3 , TiO_2 for spinel). Grey box in (a) highlights the range of CaO contents that have been independently determined for olivine cores by LA-ICP-MS. MI=estimated original melt inclusion composition (i.e., whole-rock composition minus the bulk of phenocryst compositions; see also Fig. 2); A=andesite, D=dacite, R=rhyolite, TD=trachydacite, and T=trachyte fields in the TAS diagram of Le Maitre (1976). All data are reported in Table S2. We note that the relatively large scatter in minor element concentrations (e.g., Ca for olivine) at least partly reflects that our analyses were performed at relatively low beam currents (6–10 nA) and acceleration voltages (15 keV).

Olivine, orthopyroxene, and plagioclase show normal zoning with unzoned cores; orthopyroxene and plagioclase also occasionally show round resorbed cores with normally zoned overgrowths (<1–2% of all crystals). Clinopyroxene is characterized by sector zoning and normally zoned rims. Euhedral spinel inclusions with maximum dimensions of ~10 μm are relatively common, which are typically hosted by olivine. Alteration is limited, but olivine in some samples shows iddingsite along grain boundaries and micro fractures.

The unzoned phenocryst cores, which we have used for constraining crystallization parameters, show limited compositional range (Figure 4 and Table S2). (1) Olivine cores have ~Fo75–83 and ~0.1–0.3 wt% CaO, (Figure 4a). They have ~3.6–14.9 ppm V, ~3.5–6.7 ppm Sc, and ~0.15–0.36 ppm Y, where V contents increase from olivine in the Menluhe lavas over crystals in the Xunke lavas to olivine in the Wuchagou lavas (Figure 4b). (2) Orthopyroxene cores have ~76–82% En, variably high Al_2O_3 (~1.0–3.2 wt%) and Ws (~2.5–4.5%; Figures 4c and 4d). (3) Plagioclase cores have ~40–60% An with high Or contents (~1.5–4.5%) in the Menluhe and Xunke lavas and low Or contents (<1.5%) in the Wuchagou lavas (Figure 4e). (4) Cores of the spinel inclusions are Al, Cr-, and Mg-rich and Ti- and Fe-poor (Figures 4f–4h). Clinopyroxene compositions were not systematically evaluated, given that the sector zoning of the crystals makes thermobarometric estimates problematic (e.g., Hammer et al., 2016). Melt compositions estimated to have been in equilibrium

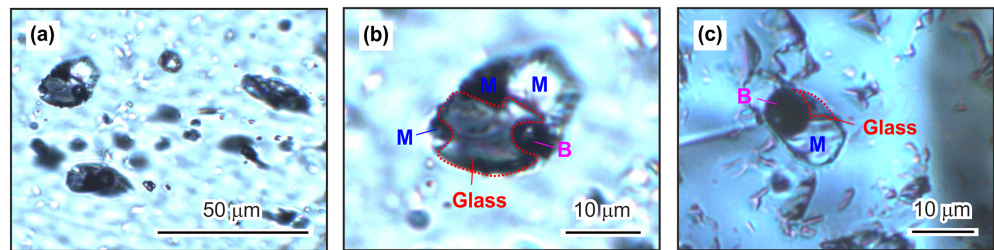


Figure 5. Microphotographs of characteristic melt inclusion textures in olivine (taken in transmitted light with partly crossed polarizer). (a) Many melt inclusions have approximately ellipsoidal, but nevertheless variable shape. (b) Close up of microphotograph in (a) showing that the melt inclusions have abundant microlites (M) and mostly relatively low glass and bubble (B) volumes. (c) Melt inclusion with a bubble that apparently makes up >10 vol%.

with the phenocryst cores are andesitic to trachy-andesitic (Figure 4i) with ~112–154 ppm V, ~11.3–17.4 ppm Sc, and ~17.9–28.9 ppm Y (Table S2). Residual glasses in the melt inclusions are, however, trachytic to trachydacitic in the Menluhe and in the Xunke samples (Figure 4i) and dacitic to rhyolitic in the Wuchagou samples (Figure 4i). The difference between inferred entrapment and residual melt compositions (Figure 4i) and optical observations (Figure 5) indicate ~50–60 vol% postentrapment crystallization.

4.3. Thermobarometric, Hygrometric, and Oxybarometric Estimates

The calculated mineral-melt partition coefficients for phenocryst cores and estimated equilibrium melts (~ground mass composition) are (1) ~0.16–0.33 for plagioclase-melt Ca-Na, (2) ~0.23–0.36 for olivine-melt Fe-Mg, and (3) ~0.22–0.34 for orthopyroxene-melt Fe-Mg for melt $\text{Fe}_2\text{O}_3/\text{FeO}$ values of ~0.19–0.39 (~FMQ +1.3 to ~FMQ+0.1), which are magmatic equilibrium values (cf. Grove et al., 2003; Putirka, 2008; Tables 1 and S2). We stress that the estimated melt compositions closely approach, but not perfectly match the true equilibrium melt compositions, which must have been slightly more primitive, that is between the ground-mass and bulk rock compositions (i.e., between our preferred and reported extreme values; Table S2). Our temperature estimates may therefore be slightly too low (by <30 °C) and our melt H_2O and $f\text{O}_2$ estimates may be slightly too high (by <0.6 wt% and <0.4 log units). The Menluhe and the Xunke orthopyroxene core compositions calculate higher pressures (on average ~520 and ~640 MPa) than the Wuchagou orthopyroxene cores (on average ~330 MPa), but the calculated values overlap within the large uncertainty of the method (± 260 MPa). The calculated phenocryst crystallization temperatures closely compare for all three systems, ranging between ~1090 and ~1200 °C with average values of ~1130–1160 °C (Tables 1 and S2). Plagioclase-melt compositions calculate low melt H_2O contents of ≤ 1.4 wt% and on average ~0.5–0.6 wt% (Tables 1 and S2). Vanadium contents of olivine and its host matrix indicate equilibration at ~FMQ+1.7 to ~FMQ+0.1 (Tables 1 and S2), and thus partial crystallization at relatively oxidizing conditions. Spinel-olivine Fe^{2+} -Mg partition coefficients vary between ~1.7 and 6.9, and they are thus high compared to high-temperature magmatic equilibrium values of ≤ 2.0 for $\geq \text{Fo}75$ olivine (cf. Gaetani & Grove, 1998; Pichavant & Macdonald, 2007), indicating that most of the spinel inclusions have experienced partial low-temperature re-equilibration. Spinel-olivine pairs that approach equilibrium compositions (with $K_D(\text{Fe}^{2+}/\text{Mg}) \leq 3.0$; Tables 1 and S2) calculate oxygen fugacities of ~FMQ+0.9, ~FMQ+0.7, and ~FMQ for the Menluhe, Xunke, and Wuchagou lavas, respectively, and thus conditions equivalent to those estimated on the basis of olivine-melt V partitioning. For the calculated temperature-pressure- H_2O - $f\text{O}_2$ conditions, thermodynamic modeling using the PELE software (Boudreau, 1999) predicts phase assemblages, phase proportions, and phase compositions that closely match those of the natural lavas (Figure S2).

4.4. Melt Inclusion Textures and Vapor Bubble CO_2

Most melt inclusions (>90%) in the Menluhe, Xunke, and Wuchagou phenocrysts comprise single vapor bubbles, while few contain multiple bubbles. Some melt inclusions are large and irregular, while others approach ellipsoidal shape. The melt inclusions have faceted walls and typically contain large volumes of microlites (~40–60%). The inferred volumes of the approximately ellipsoidal melt inclusions (i.e., inclusion space made up of microlites, glass, bubble, plus optically visible walls; Figure 5) are <25,000 μm^3 and their bubble volumes are <500 μm^3 (Figure 6a). Most of the vapor bubbles make up ~1–6 vol% and on average ~3 vol% of the inclusions (Figures 6a and 6b). Others, however, occupy up to ~75 vol% of the inclusion space

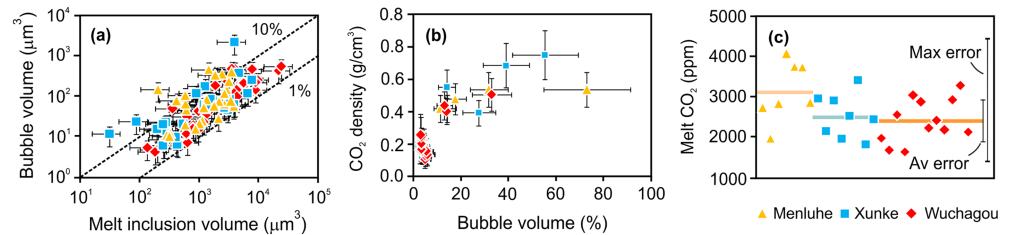


Figure 6. Melt inclusion textures and composition. (a) Volume proportions of melt inclusions and their vapor bubbles. The dashed lines mark where bubbles make up 1 and 10% of the melt inclusions. (b) Variation of CO_2 vapor density as a function of bubble volume. (c) Range of estimated entrapment melt CO_2 content for individual melt inclusions and their average compositions ($\sim 3,100$, $\sim 2,500$, and $\sim 2,400$ ppm) for the Menluhe, Xunke, and Wuchagou lavas (indicated by the yellow, red, and blue lines). Estimated average (Av) and maximum (Max) errors.

(Figures 6a and 6b). Low-density vapor was detected in bubbles that make up ~ 1 –6 vol% with CO_2 densities of ~ 0.21 (0.15 – 0.24) g/cm^3 in the Menluhe, ~ 0.16 (0.12 – 0.21) g/cm^3 in the Xunke, and ~ 0.17 (0.11 – 0.26) g/cm^3 in the Wuchagou samples; high-density CO_2 (≥ 0.39 – 0.75 g/cm^3) was detected in some of the bubbles that make up >10 vol% of the inclusions (Figure 6b and Table S3). Many of the analyzed vapor bubbles ($\geq 80\%$), however, yielded no detectable volatile signals, indicating late, low-pressure entrapment and/or that CO_2 was lost along common micro fractures and cleavage planes during the <1 to ~ 11 Ma lifetime of the samples.

5. Discussion

5.1. Crustal Magma Evolution

Intermittent crustal residence of the Menluhe, Xunke, and Wuchagou magmas is recorded by the presence of phenocrysts with unzoned core plateau zones, which are inferred to record crystallization during short-term magma arrest. Rare plagioclase and orthopyroxene crystals that show round, resorbed cores are interpreted as antecrysts, but they are a minor component (<1 – 2% of all crystals). The high temperatures calculated for the partial crystallization of the basaltic andesitic and andesitic magmas (Figure 7a and Tables 1 and S2) and their low phenocryst content rules out significant crustal assimilation during intermittent storage or ascent. The rare quartz and plagioclase xenocrysts (<1 vol%) that are present in some of our samples were likely

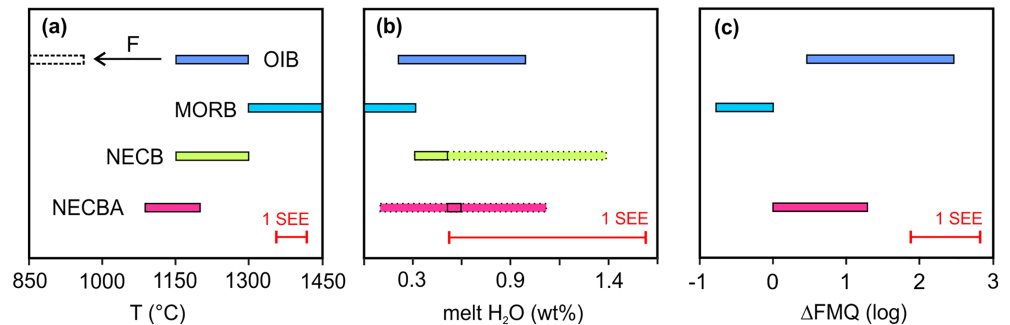


Figure 7. Summary of pre-eruptive (a) temperatures, (b) undegassed melt H_2O contents, and (c) redox conditions (expressed as ΔFMQ) estimated for magmas of the three studied systems (basaltic andesites and andesite from Northeast China; NECBA) in comparison to those inferred for ocean island and ocean plateau basaltic magmas (summarized as OIB) and their fractionates (F), mid-ocean-ridge basaltic magmas (MORB), and Cenozoic basaltic magmas erupted above the big mantle wedge in Northeast China (NECB). Data for OIBs and their fractionates are from Andújar et al. (2010), Coogan et al. (2014), Dixon et al. (2002), Foley (2011), Gaillard et al. (2015), Helz and Thornber (1987), Hirschmann (2006), Keiding and Sigmarsson (2008), Martel et al. (2013), Moussallam et al. (2013), Wallace (2005), and Xia et al. (2017); data for MORBs are from Bézoz and Humler (2005), Coogan et al. (2014), Dixon et al. (2002), Hirschmann (2006), Wallace (2005), and Xia et al. (2017); data for NECB are from Chen, Xia, and Ingrin (2015), Chen, Xia, Ingrin, Jia, et al. (2015), Kuritani et al. (2013), Liu, Xia, Deloule, Chen, et al. (2015), Liu, Xia, Deloule, Ingrin, et al. (2015), Zhang et al. (2016), and Xia et al. (2017). Melt H_2O contents estimated for NECB are mostly ~ 0.3 – 0.5 wt% (solid outline), but extend to estimates of up to ~ 1.4 wt% (stippled outline). Estimated average melt H_2O contents for the studied systems are ~ 0.5 – 0.6 wt%, but calculated values show a larger range if individual hygrometers are considered (stippled outline; see details in Table 1). Standard errors of the estimates (SEEs) are as indicated or lower.

entrained at the surface following eruption, as they would not have survived resorption otherwise. Evidence for the presence of mantle xenocrysts, in contrast, is lacking, for example, olivine with <0.1 wt% CaO was not detected. Partial resorption of orthopyroxene (in all samples) and \pm olivine (in the Wuchagou samples) by low-Mg clinopyroxene (Figure 3) is inferred to record peritectic reaction at low pressure and low temperature during magma ascent and/or extrusion, as predicted by our thermodynamic modeling (Figure S2).

5.2. High-Temperature, Mantle-Derived Melts

The pre-eruptive temperatures calculated for the macrophenocryst cores of all three systems are \sim 1090–1200 °C and \sim 1130–1160 °C on average (Tables 1 and S2 and Figure 7a). Given that the estimates closely compare for all four employed thermometers, we consider them to be accurate and precise (i.e., they are clearly within the standard errors of the methods of \pm 15–50 °C and below estimated maximum errors, which limits the uncertainties of our barometric, hygrometric, and oxybarometric estimates). We highlight, however, that the calculated temperatures could be slight underestimates (by <30 °C), because the mineral cores must have been in equilibrium with a melt that was slightly more primitive than our estimated equilibrium melt composition (i.e., between groundmass and bulk-rock composition and between preferred and extreme values, details in Table S2). The estimated temperatures are high (higher by \geq ~150 °C) compared to those of typical, hydrous arc basaltic andesites and andesites (which are stored at \leq 950–1000 °C prior to eruption, e.g., at Mount Merapi, Indonesia, or Mount Pelée, Lesser Antilles; Erdmann et al., 2016; Pichavant et al., 2002), yet approach those of dry to H₂O-poor, aphyric basalt erupted at ocean plateaus or ocean islands (\geq 1150 °C; Coogan et al., 2014; Helz & Thornber, 1987; Keiding & Sigmarsson, 2012). Most importantly, our estimated temperatures of partial crystallization (\sim 1090–1200 °C or slightly higher) are close to those estimated for aphyric potassic basalts (\sim 1150–1300 \pm 50 °C) that have erupted at various locations around the Songliao Basin (Kuritani et al., 2013; Zhang et al., 2016; Figure 1a; and 7a).

The high calculated pre-eruptive temperatures of the basaltic andesitic and andesitic magmas are taken to record that they derived from the mantle and that they have experienced limited crustal assimilation. The pre-eruptive temperatures calculated for the basaltic andesites and andesites are lower by \leq 60–200 (likely \sim – \leq 100) °C compared to those of the potassic basalts erupted around the Songliao basin, where part of the apparent temperature difference could reflect uncertainties of the applied thermometers (\sim \pm 50 °C). We nevertheless consider that the basaltic andesitic and andesitic magmas had lower pre-eruptive temperatures than the spatiotemporally associated basaltic magmas, which could indicate that the Menluhe, Xunke, and Wuchagou magmas formed by fractionation of more primitive magmas, for example, magmas close in composition to basalts erupted around the Songliao basin. Most major- and minor-element contents of the basaltic andesitic and andesitic lavas plot as an extension of the compositional trends defined by Cenozoic basalts from Northeast China (Figure 8), but modeling shows that fractionation of the potassic or sodic basaltic magmas through olivine, \pm plagioclase, \pm clinopyroxene, \pm oxide, \pm apatite crystallization does not produce liquids that match or closely approach the SiO₂, TiO₂, MgO, or K₂O composition of the basaltic andesites or andesites (Figure 2, where cooling by up to a maximum of 200 °C is considered). The studied lavas are SiO₂- and MgO-rich yet TiO₂- and K₂O-poor compared to the liquid fractionates (Figures 2a, 2d, and 2h). We therefore posit that the basaltic andesites and andesites represent high-temperature, mantle-derived melts that have experienced no or limited fractionation. Their lower pre-eruptive temperatures compared to the spatiotemporally associated basalts may reflect slower ascent and a larger degree of cooling en route to the surface, owing to a higher viscosity of the evolved magmas.

5.3. CO₂- and H₂O-Poor Magmas

Melt inclusions with vapor bubbles that make up large proportions of the inclusion space (i.e., vapor bubbles that make up $>$ ~8–10 vol%), as some in the phenocrysts of our samples (Figures 5c and 6b and Table S3), may record the entrapment of two-phase liquids (silicate melt and an exsolved vapor phase), but they may also record decrepitation or leakage (cf. Bodnar & Student, 2006; Moore et al., 2015; Steele-MacInnis et al., 2017). The presence of high-density CO₂ (\sim 0.39–0.75 g/cm³) in some of the high-volume vapor bubbles (Figure 6b and Table S3) suggests that a two-phase liquid was indeed locally trapped (cf. Steele-MacInnis et al., 2017), and thus that the Menluhe, Xunke, and Wuchagou systems were volatile saturated during phenocryst crystallization. Bubbles in melt inclusions that occupy only \sim 1–6 vol% and on average \sim 3 vol% of the melt inclusion space, in contrast, are interpreted to have formed by postentrapment cooling (cf. Lowenstern, 1995; Roedder, 1979; Steele-MacInnis et al., 2011; Wallace, 2005). Their low-density CO₂ is interpreted to

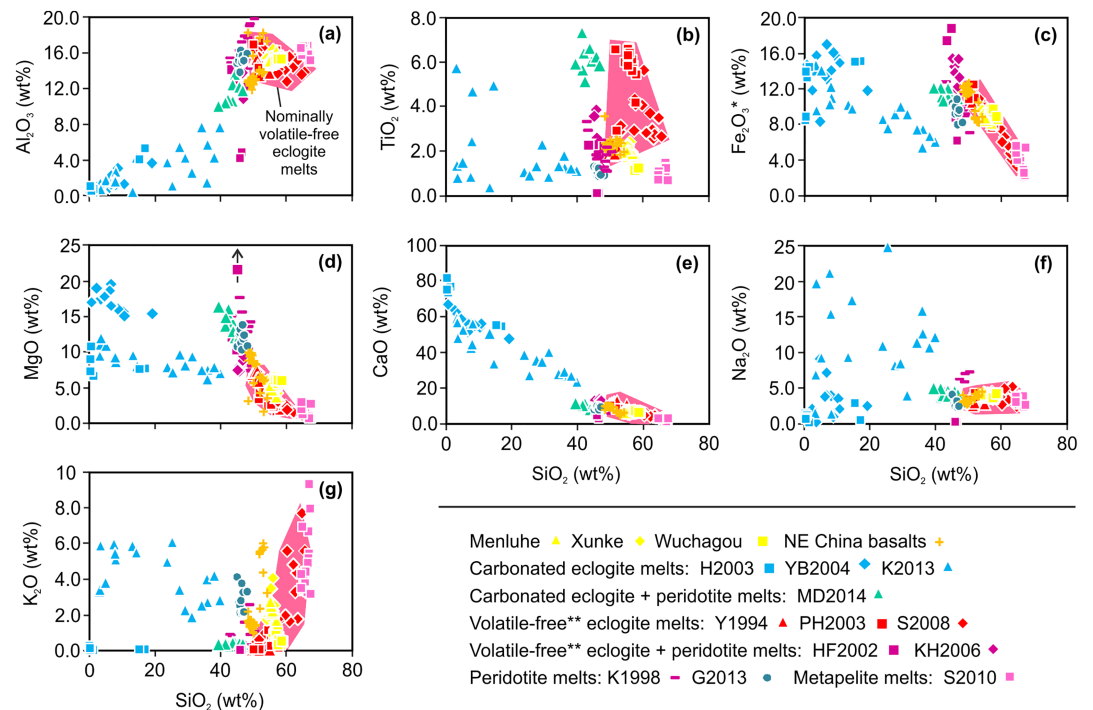


Figure 8. Composition of the Menluhe, Xunke, and Wuchagou basaltic andesites and andesites (yellow symbols) compared to the composition of basalts from Northeast (NE) China and compared to melts produced in high-pressure, high-temperature experiments (all data normalized to 100%). The composition of the Menluhe, Xunke, and Wuchagou lavas closely compares to nominally anhydrous eclogite partial melts (red fields), while they have significantly higher SiO_2 and lower MgO than peridotite-derived or carbonated melts (with <50 wt% SiO_2). The vertical arrow in (d) highlights that some peridotite-derived partial melt is outside the compositional range shown, with $\sim 36\text{--}40$ wt% MgO. *All Fe shown as Fe_2O_3 . **Nominally volatile-free experiments, which inevitably contain minor to trace amounts of volatiles. Experimental compositions are from: H2003=Hammouda (2003); YB2004=Yaxley and Brey (2004); K2013=Kiseeva et al. (2013); MD2014=Mallik and Dasgupta (2014); Y1994=Yasuda et al. (1994); PH2003=Pertermann and Hirschmann (2003); S2008=Spandler et al. (2008); HF2002=Hirose and Fei (2002); KH2006=Kogiso and Hirschmann (2006); S2010=Spandler et al. (2010); G2013=Grove et al. (2013); K1998=Kogiso et al. (1998). Compositions of NE China basalts are for the Wudalianchi, Halaha, and Changbaishan volcanic centers; data are from Kuritani et al. (2013), Ho et al. (2013), and Andreevaa et al. (2014).

have exsolved from the trapped melt during magma ascent and cooling (cf. Bodnar & Student, 2006; Esposito et al., 2014; Hartley et al., 2014; Moore et al., 2015). For the low-volume vapor bubbles filled with low-density CO_2 , we assume that all but traces of CO_2 degassed from the melt into the bubbles of the inclusions, which we deem inevitable given the slow cooling of the lavas recorded by their coarse-grained groundmass (e.g., Figure 3) and by significant post-entrapment melt inclusion crystallization (Figure 5). This then indicates entrapment melt CO_2 contents of $\sim 1,600\text{--}4,100$ ppm and on average $\sim 2,400\text{--}3,300 \pm 500$ ppm. At saturation, such CO_2 contents indicate entrapment pressures of >300 and <600 MPa and on average $\sim 420\text{--}520 \pm 50\text{--}100$ MPa using the solubility model of Papale et al. (2006; Table 1). The calculated entrapment melt CO_2 contents provide a minimum estimate for the CO_2 contents of the parental magmas, as CO_2 may have partially degassed during ascent in crust or mantle. CO_2 contents of a few thousand ppm as those inferred are, however, characteristic for undegassed, enriched parental magmas of ocean island basalts and ocean plateau basalts (e.g., those that have erupted at La Réunion or Galapagos; Rosenthal et al., 2015; Wallace, 2005).

The calculated melt H_2O contents of $\sim 0.5\text{--}0.6 \pm 0.4\text{--}1.0$ wt% moreover suggest partial crystallization at H_2O -poor conditions; comparing the values calculated using mineral core compositions and estimated groundmass composition or bulk-rock composition, respectively (preferred and extreme values in Table S2), further indicates that these values are likely maximum estimates. The two employed hygrometers calculate slightly different melt H_2O contents ($\sim 0.1\text{--}0.6$ and ~ 0.5 to 1.0 wt%, respectively), but the values are well within the standard errors of $\pm 0.4\text{--}1.0$ wt%. Maximum errors of up to $\pm 1.2\text{--}2.2$ wt% are possible, but

unlikely given plagioclase-melt equilibrium and our fairly tight constraints on crystallization temperature. As for CO_2 , the melt H_2O contents of the basaltic andesites and andesites are in the range of those typical for ocean island and ocean plateau basalts ($\sim 0.2\text{--}1.0$ wt%), yet tend to higher H_2O than typical mid-ocean-ridge basaltic magmas (with ≤ 0.3 wt% H_2O ; Dixon et al., 2002; Hirschmann, 2006; Wallace, 2005; Xia et al., 2017; Figure 7b). They also compare to melt H_2O contents of $\sim 0.3\text{--}0.5$ wt% that have been estimated for spatially and temporally associated potassic basalts erupted at Xiaogulihe and to melt H_2O contents estimated for sodic basalts erupted in the Taihang mountains (Figure 1a), where estimates are based on the H_2O content of clinopyroxene phenocrysts and clinopyroxene-melt H_2O partitioning (Chen, Xia, & Ingrin, 2015; Chen, Xia, Ingrin, Jia, et al., 2015; Liu, Xia, Deloule, Chen, et al., 2015; Liu, Xia, Deloule, Ingrin, et al., 2015; Xia et al., 2017). Others have inferred maximum melt H_2O contents of $\sim 1.1\text{--}1.4$ wt% for at least some of the potassic basalts (erupted at Wudalianchi, Figure 1a; Kuritani et al., 2013), which are slightly higher values, but within the uncertainty of all other estimates. Melt H_2O contents higher than those characteristic for depleted, mantle-derived melts (typically ≤ 0.3 wt%), yet still relatively low melt H_2O contents (i.e., $\sim \leq 1$ wt%), appear thus to be typical for the magmas erupted above the big mantle wedge of the Pacific plate and west of it. Parental melts with such H_2O contents are inferred to be derived from mantle sources with $\sim \leq 1,000$ ppm H_2O (cf. Hirschmann, 2006) or less (Kimura et al., 2018).

5.4. Oxidized Magmas and Mantle Sources

That both olivine-melt V compositions and spinel-olivine pairs calculate closely comparable redox conditions of $\sim \text{FMQ}+1.3$ to $\text{FMQ}+0.1$ (Tables 1 and S2) gives us confidence that the estimates are realistic, while we consider uncertainties of up to ± 1 log unit. We further consider that the calculated values may slightly overestimate oxidation, especially if minor fractionation of olivine and pyroxenes occurred (by < 0.4 log units; see preferred versus extreme values in Table S2). That the phase compositions calculate increasingly reducing conditions from the Menluhe over the Xunke to the Wuchagou system may be significant, but it may also be an artifact of the system/magma compositional variation, which has to be further evaluated. The calculated conditions are close to, but they are more oxidized than those characteristic for MORB-type magmas derived from depleted mantle sources (typically $\sim \text{FMQ}-0.4 \pm 0.4$; Bézoz & Humler, 2005), yet compare to the more oxidized redox state characteristic for many intraplate magmas (with $\sim \text{FMQ}+0.5$ to $\sim \text{FMQ}+2.5$; Foley, 2011; Gaillard et al., 2015; Moussallam et al., 2016; Oppenheimer et al., 2011; Figure 7c). Most recent studies moreover suggest that the redox state of mantle-derived magmas approaches that of their sources within ~ 1 log unit at least prior to significant sulfur degassing at shallow level (at $\leq \sim 200$ MPa; e.g., Gaillard et al., 2015) and unless they have experienced significant melt-rock reaction. We infer olivine-melt and spinel-olivine equilibration for phenocrysts cores and thus $f\text{O}_2$ of the magmas for partial crystallization during intermittent storage at $\geq \sim 400$ MPa (Table 1), in which case degassing-related $f\text{O}_2$ variation should have had no large effect on our estimates. The effect of melt-rock reaction on the redox state of the magmas remains unconstrained; it would have reduced the melts if they were H_2O -poor, as the normal upper mantle beneath eastern China is inferred to be buffered at $\leq \text{FMQ}-1.5$ to FMQ (Li & Wang, 2002), but could have oxidized them if they were H_2O -rich (e.g., Tollan & Hermann, 2019). We therefore propose that the Menluhe, Xunke, and Wuchagou magmas were either derived from mantle sources at $\sim \text{FMQ}-1 \pm 1$ to $\sim \text{FMQ} \pm 1$, and thus from comparatively oxidized mantle domains compared to typical asthenosphere at $< \text{FMQ}-1$ to $\sim \text{FMQ}-3$ (Foley, 2011), or that the melts acquired a relatively oxidized signature during ascent in the mantle as a result of H_2 loss.

5.5. Volatile-Poor, Eclogite-Rich Magma Sources

The basaltic andesitic and andesitic magmas have $\text{SiO}_2/\text{TiO}_2$, SiO_2/MgO , and $\text{SiO}_2/\text{K}_2\text{O}$ compositions that are unlike those of possible fractionates of basalts that have erupted in spatiotemporal association (Figure 2), and we therefore rule out a direct genetic relation between the basaltic and the studied basaltic andesitic and andesitic magmas. The SiO_2 contents of the lavas studied are moreover significantly above and the MgO contents are significantly below those generated by peridotite melting (Figure 8). An early study has suggested that the Wuchagou lavas may represent tholeiitic melts produced by lherzolite partial melting that have assimilated significant amounts of lower crust (Ho et al., 2003). This proposal can, however, be ruled out on the basis of thermal considerations, given that the temperatures of the erupted magmas were high ($\sim 1130\text{--}1160$ °C), while assimilation would have significantly reduced them (e.g., relative to the basaltic magmas erupted in the area). Lim et al. (2017) interpret the SiO_2 -rich ($\sim 57\text{--}59$ wt%) Wuchagou lavas to represent asthenosphere-derived melts formed by partial melting of eclogite, which experienced no

significant crustal contamination yet limited reaction with peridotite. Like the Wuchagou andesites, major-element compositions of the Menluhe and Xunke basaltic andesites and andesites compare to (1) the composition of experimental melts derived from nominally anhydrous and CO₂-free mafic eclogite and they are (2) intermediate to the major-element compositions of experimental melts derived from nominally anhydrous and CO₂-free sedimentary eclogite and peridotite-derived melts (Figure 8). Trace to minor amounts of H₂O and CO₂, as we infer them for the natural systems, were very likely present in the experiments (they are inevitable contaminants; e.g., Spandler et al., 2008), while higher volatile contents (i.e., >1 wt% combined) can be ruled out for the experimental systems and thus also for the sources of our investigated natural systems. Spatiotemporally associated sodic basalts are interpreted to derive from depleted mantle sources with minor contributions from enriched components, while spatiotemporally associated potassic basalts erupted at Wudalianchi, Nuominhe, and Xiaogulihe, have long been interpreted to comprise partial melts derived from metasedimentary eclogite with contributions of depleted mantle through reaction or metasomatism (Liu et al., 2016; J.-Q. Liu et al., 2017; Wang et al., 2017). The basaltic andesite and andesite lava compositions are closest to the composition of eclogite-derived melts, that is, closer than the composition of the potassic basalts, which are in turn closer to eclogite-derived melt composition than the sodic basalts, which is consistent with the interpretation that the sources of the potassic basalts comprise eclogite and that the sources of the basaltic andesites and andesites comprise an even higher proportion of eclogite (cf. Figure 8).

The comparable major- and minor-element composition of the Menluhe and Xunke lavas (Figure 2) indicate that they derive from similar sources and that they have undergone a similar evolution, while the larger compositional variation of the Xunke samples records a more complex source origin and/or evolution. However, high Al₂O₃/SiO₂, low MgO/SiO₂, and uncorrelated CaO/SiO₂ and Na₂O/SiO₂ for the Menluhe and Xunke samples, on one hand, and low Al₂O₃/SiO₂, high MgO/SiO₂, and correlated CaO/SiO₂ and Na₂O/SiO₂ for the Wuchagou samples, on the other hand (Figures 2b, 2d, 2f, and 2g), rule out that the lavas from all three volcanic centers represent a liquid line of descent. The Wuchagou lavas have SiO₂, Al₂O₃, Fe₂O₃, CaO, and Na₂O compositions that closely match those of mafic eclogite-derived melts (Figures 8a, 8c, 8e, and 8f; Spandler et al., 2010). The relatively tight oxide correlation trends for the Wuchagou lavas with >57.5 wt% SiO₂ that show increasing Al₂O₃, Na₂O, K₂O, and P₂O₅ (Figures 2b, 2g, 2h, and 2i) and decreasing Fe₂O₃, MnO, CaO (Figures 2c, 2e, and 2f) could reflect minor crystal fractionation, but inferred liquid compositions diverge from the whole-rock compositional trends (Figure 2), arguing against fractionation at crustal level. The compositional trends could instead represent magmas derived from slightly higher- to slightly lower-degree eclogite partial melting (e.g., melt fractions of ~30 versus ~20 wt% for a mafic eclogite), while an increase in Al₂O₃ with increasing SiO₂ (Figure 2b) is unexpected (cf. Spandler et al., 2010). The Wuchagou lavas are moreover notably low in TiO₂, K₂O, and P₂O₅ (Figures 8b and 8g, not shown for P₂O₅), while their MgO content is significantly higher (~6 wt%; Figure 8d) than MgO contents of typical mafic or sedimentary eclogites (~4–1 wt%) formed at estimated mantle potential temperatures of ≥1250–1350 °C and ≥2.5 GPa (Pertermann & Hirschmann, 2003; Spandler et al., 2010). MgO contents of eclogitic melts increase with increasing formation pressure (e.g., Spandler et al., 2008, 2010), but such an effect alone cannot explain the high-MgO signature. The high MgO, low TiO₂, K₂O, and P₂O₅ signature is commonly interpreted to record melt-peridotite reaction during melt ascent (Mallik & Dasgupta, 2014; J.-Q. Liu et al., 2017), but could also partly record partial diffusive re-equilibration between eclogite source components (e.g., lenses) and their peridotite host during protracted mantle residence (Smart et al., 2009). Additional processes must, however, have controlled MgO/SiO₂ of the studied magma systems, given the overall lack of negative correlation between MgO and SiO₂ (Figure 2d). The Menluhe and Xunke lavas with low SiO₂ and MgO (Figure 2d), and notably high TiO₂, Al₂O₃, K₂O, and P₂O₅ (Figures 2a, 2b, 2h, and 2i) compared to the Wuchagou lavas could derive from eclogite sources that differed in composition from those that fed the Wuchagou volcanism. The compositional differences could alternatively – or in addition – record that the Menluhe and Xunke magmas formed by lower-degree partial melting of an eclogite source similar to that of the Wuchagou magmas, while additional reaction processes during melt segregation and/or ascent would then be needed to explain the low SiO₂ and relatively high TiO₂, Al₂O₃, and Na₂O contents (cf. Figure 2b). We conclude that the Wuchagou, Xunke, and Menluhe lavas have a significant volatile-poor, eclogite source component, but highlight that trace-element and isotopic data are needed to investigate the similarity/dissimilarity of their sources, to estimate variation in the degree of source partial melting, and to reconstruct and quantify reaction(s) with peridotite and other lithologies.

5.6. Upwelling of Oxidized and Enriched Mantle Beneath Eastern China

Upwelling mantle beneath Eastern China with low- V_P , low- V_S character has commonly been invoked to be hydrous, hydrous and hot, or hot and only weakly hydrous (Chen et al., 2017; Kimura et al., 2018; Kuritani et al., 2011, Kuritani et al., 2013, Kuritani et al., 2019; Wei et al., 2019). Experimental work has shown that the presence of hydroxyl (dissolved “H₂O”) does not significantly decrease seismic velocities of peridotite (e.g., by <1% for a 1 wt% increase in dissolved H₂O), while high temperature (Cline et al., 2018; Karato, 2011) and the presence of partial melt or free volatiles do (Aizawa et al., 2008; Cline et al., 2018; Karato, 2011). It has been proposed that upwelling plumes are melt-bearing from the mantle transition zone to the surface (Kuritani et al., 2019), while most studies advocate that significant, but nevertheless, low-volume partial melting takes place at asthenosphere level, where the presence of partial melting likely contributes to some of the recorded low-velocity seismic anomalies (e.g., those shown in the studies of Chen et al., 2017; Huang & Zhao, 2006; Kimura et al., 2018; Wei et al., 2019; Figure 1b). The melt-bearing parts of mantle plumes may account for seismic low-velocities; other factors that significantly control seismic wave speeds are mantle redox state and major-element composition, where velocities are reduced in oxidized lithologies and in eclogite relative to peridotite (Behn & Kelemen, 2003; Cline et al., 2018; Karato, 2011). Given the importance of enriched, eclogitic source components in Eastern China’s Cenozoic magmatism (Liu et al., 2016; J.-Q. Liu et al., 2017; Wang et al., 2017; Xu et al., 2018) and the oxidized character of the magmas and their sources studied here, we suggest that redox state and enriched components (e.g., eclogite dispersed in peridotite) significantly contribute to the characteristic low- V_P , low- V_S anomalies that have been imaged in regional and local seismic tomography experiments. Further studies are needed to assess the redox state of other Cenozoic lavas erupted in Eastern Asia and their mantle sources to evaluate the overall importance of oxidized mantle domains and any possible spatial variation, while we stress that recycled components are commonly invoked to produce long-lived oxidized mantle domains (e.g., Foley, 2011; Gaillard et al., 2015).

We highlight that we do not rule out that upwelling, melt-producing mantle beneath Eastern China is more hydrous than the ambient mantle, as has been suggested by many studies (Kuritani et al., 2011, 2013; Tang et al., 2014; Wei et al., 2019; Xu et al., 2018). Given that the mantle transition zone below Eastern Asia appears to be extremely hydrous with ~0.1–0.4 wt% H₂O or more (Kelbert et al., 2009), it is possible that upwelling mantle produces partial melts at the top of the mantle transition zone (cf. Bercovici & Karato, 2003), as has been proposed by Tauzin et al. (2017) and Wei et al. (2019). This depletes and dries upwelling mantle, while the upwelling mantle domains may nevertheless remain more enriched and more hydrous than the surrounding upper mantle. Our key point is that mantle hydration has a relatively insignificant effect on seismic velocities (cf. Cline et al., 2018; Karato, 2011) unless melt is present and that we suggest that redox state and composition significantly contribute to the low seismic velocities beneath Eastern Asia, likely in combination with high temperatures of the upwelling zones (e.g., Kimura et al., 2018).

6. Conclusions

We infer (1) that the basaltic andesitic and andesitic magmas erupted at the Cenozoic Menluhe, Xunke, and Wuchagou volcanic centers were hot (~1130–1160±15–50 °C), volatile-poor (~2,400–3,100±500 ppm CO₂, ~0.5–0.6±0.4–1.1 wt% H₂O), and relatively oxidized (at ~FMQ+1.3 to ~FMQ±1.0), comparing in these intensive parameters to typical ocean island and ocean plateau basalts, and (2) that the basaltic andesitic and andesitic magmas were generated by partial melting of relatively oxidized (~FMQ–1 to ~FMQ±1.0), CO₂- and H₂O-poor, eclogite components in the upper mantle. We suggest that enriched mantle components, which are known to be abundant beneath eastern China, and oxidized mantle domains as those inferred, significantly contribute to the low P and S wave velocity anomalies that have been detected by seismic tomography. This is important for further interpreting material flux above and around the stagnant Pacific slab, as previous studies have interpreted the low velocity anomalies to outline hydrous, hot and hydrous, or mostly hot domains. The upwelling domains may be, but do not have to be relatively hydrous. If temperature differences significantly contribute to the observed low- and high-velocity P and S wave anomalies largely depends on where the upwelling mantle originates, that is, at the relatively cold top of the mantle transition zone or at hotter, deeper levels, which needs to be further evaluated. Detailed petrological-geochemical studies are moreover needed to unravel if the various seismic anomalies above and beyond the big mantle wedge

beneath Eastern Asia represent similarly enriched, and oxidized mantle, or if characteristic variation exists between zones close to and distal from the subduction zone.

Data

Supporting Information files available at the publisher site provide detailed method descriptions (Texts S1 to S7 and Figures S1 and S2). Supplementary tables that provide all our data (Tables S1 to S3 with whole-rock major-element compositions, mineral compositional data and calculated intensive parameters, and melt inclusion data) are available at Figshare (<https://doi.org/10.6084/m9.figshare.9861662>; <https://doi.org/10.6084/m9.figshare.9861734>; <https://doi.org/10.6084/m9.figshare.9861881>).

Acknowledgments

We would like to thank two anonymous reviewers for their detailed and constructive comments and Editor Marie Edmonds for her efficient handling of our submission. We also thank Zhang Wenlan and Ida Di Carlo for support with the microprobe analyses and Abdeltif Ladtif, Ida Di Carlo, Junying Ding, and Zheng Liu for the introduction to and for support with the micro Raman analyses. This study was financially supported by the National Natural Science Foundation of China (grants 41688103 and 41672049). S. E. was supported by a Nanjing University postdoctoral fellowship during part of the study.

References

- Aizawa, Y., Barnhoorn, A., Faul, U. H., Fitz Gerald, J. D., Jackson, I., & Kovács, I. (2008). Seismic properties of Anita Bay dunite: An exploratory study of the influence of water. *Journal of Petrology*, *49*, 841–855. <https://doi.org/10.1093/ptrology/egn007>
- Andreevaa, O. A., Yarmolyuka, V. V., Andreevaa, I. A., Jib, J. B., & Lib, W. R. (2014). The composition and sources of magmas of Changbaishan Tianchi Volcano (China–North Korea). *Doklady Earth Sciences*, *456*, 572–578. <https://doi.org/10.1134/S1028334X14050213>
- Andújar, J., Costa Rodríguez, F., & Marti, J. (2010). Magma storage conditions of the last eruption of Teide volcano (Canary Islands, Spain). *Bulletin of Volcanology*, *72*, 381–395. <https://doi.org/10.1007/s00445-009-0325-3>
- Behn, M. D., & Kelemen, P. B. (2003). Relationship between seismic P-wave velocity and the composition of anhydrous igneous and meta-igneous rocks. *Geochemistry, Geophysics, Geosystems*, *4*, (5), 1041. <https://doi.org/10.1029/2002GC000393>
- Bercovici, D., & Karato, S. (2003). Whole-mantle convection and the transition-zone water filter. *Nature*, *425*, 39–44. <https://doi.org/10.1038/nature01918>
- Bézos, A., & Humler, E. (2005). The Fe³⁺/ΣFe ratios of MORB glasses and their implications for mantle melting. *Geochimica et Cosmochimica Acta*, *69*, 711–725. <https://doi.org/10.1016/j.gca.2004.07.026>
- Bodnar, R. J., & Student, J. J. (2006). Melt inclusions in plutonic rocks: Petrography and microthermometry. In: *Melt Inclusions in Plutonic Rocks* (J. D. Webster, ed.). *Mineralogical Association of Canada, Short Course*, *36*, 1–26.
- Boudreau, A. E. (1999). PELE - a version of the MELTS software program for the PC platform. *Computers & Geosciences*, *25*, 201–203. [https://doi.org/10.1016/S0098-3004\(98\)00117-4](https://doi.org/10.1016/S0098-3004(98)00117-4)
- Chen, C., Zhao, D., Tian, Y., Wu, S., Hasegawa, A., Lei, J., et al. (2017). Mantle transition zone, stagnant slab and intraplate volcanism in Northeast Asia. *Geophysical Journal International*, *209*, 68–85. <https://doi.org/10.1093/gji/ggw491>
- Chen, H., Xia, Q. K., & Ingrin, J. (2015). Water content of the Xiaogulihe ultrapotassic volcanic rocks, NE China: Implications for the source of the potassium-rich component. *Science Bulletin*, *60*, 1468–1470. <https://doi.org/10.1007/s11434-015-0862-4>
- Chen, H., Xia, Q. K., Ingrin, J., Jia, Z. B., & Feng, M. (2015). Changing recycled oceanic components in the mantle source of the Shuangliao Cenozoic basalts, NE China: New constraints from water content. *Tectonophysics*, *650*, 113–123. <https://doi.org/10.1016/j.tecto.2014.07.022>
- Chen, Y., Zhang, Y. X., Graham, D., Su, S. G., & Deng, J. F. (2007). Geochemistry of Cenozoic basalts and mantle xenoliths in Northeast China. *Lithos*, *96*, 108–126. <https://doi.org/10.1016/j.lithos.2006.09.015>
- Cheng, X. Q., Zhu, J.-S., & Cai, X.-L. (2006). A study of global vertical velocity of mantle flow. *Chinese Journal of Geophysics*, *49*(4), 907–914. <https://doi.org/10.1002/cjg2.911>
- Cline, C. J., Faul, U. H., David, E. C., Berry, A. J., & Jackson, I. (2018). Redox-influenced seismic properties of upper-mantle olivine. *Nature*, *555*, 355–358. <https://doi.org/10.1038/nature25764>
- Coogan, L. A., Saunders, A. D., & Wilson, R. N. (2014). Aluminum-in-olivine thermometry of primitive basalts: Evidence of an anomalously hot mantle source for large igneous provinces. *Chemical Geology*, *368*, 1–10. <https://doi.org/10.1016/j.chemgeo.2014.01.004>
- Dixon, J. E., Leist, L., Langmuir, C., & Schilling, J.-G. (2002). Recycled dehydrated lithosphere observed in plume-influenced mid-ocean-ridge basalt. *Nature*, *420*, 385–389. <https://doi.org/10.1038/nature01215>
- Erdmann, S., Martel, C., Pichavant, M., Bourdier, J.-L., Champallier, R., Komorowski, J.-C., & Cholik, N. (2016). Constraints from phase equilibrium experiments on pre-eruptive storage conditions in mixed magma systems: A case study on crystal-rich basaltic andesites from Mount Merapi, Indonesia. *Journal of Petrology*, *57*, 535–560. <https://doi.org/10.1093/ptrology/egw019>
- Esposito, R., Hunter, J., Schiffbauer, J. D., Shimizu, N., & Bodnar, R. J. (2014). An assessment of the reliability of melt inclusions as recorders of the pre-eruptive volatile content of magmas. *American Mineralogist*, *99*, 976–998. <https://doi.org/10.2138/am.2014.4574>
- Faccenna, C., Becker, T. W., Lallemand, S., Lagabrielle, Y., Funicello, F., & Piromallo, C. (2010). Subduction-triggered magmatic pulses: A new class of plumes? *Earth and Planetary Science Letters*, *299*, 54–68. <https://doi.org/10.1016/j.epsl.2010.08.012>
- Fan, Q., & Hooper, P. R. (1991). The Cenozoic basaltic rocks of eastern China: Petrology and chemical composition. *Journal of Petrology*, *32*, 765–810. <https://doi.org/10.1093/ptrology/32.4.765>
- Foley, S. F. (2011). A reappraisal of redox melting in the Earth's mantle as a function of tectonic setting and time. *Journal of Petrology*, *52*, 1363–1391. <https://doi.org/10.1093/ptrology/egq061>
- Fukao, Y., Obayashi, M., Nakakuki, T., & The Deep Slab Project Group (2009). Stagnant slab: A review. *Annual Review of Earth and Planetary Sciences*, *37*, 19–46. <https://doi.org/10.1146/annurev.earth.36.031207.124224>
- Gaetani, G. A., & Grove, T. L. (1998). The influence of water on melting of mantle peridotite. *Contributions to Mineralogy and Petrology*, *131*, 323–346. <https://doi.org/10.1007/s004100050396>
- Gaillard, F., Scaillet, B., Pichavant, M., & Iacono-Marziano, G. (2015). The redox geodynamics linking basalts and their mantle sources through space and time. *Chemical Geology*, *418*, 217–233. <https://doi.org/10.1016/j.chemgeo.2015.07.030>
- Grove, T., Holbig, E. S., Barr, J. A., Till, C. B., & Krawczynski, M. J. (2013). Melts of garnet lherzolite: Experiments, models and comparison to melts of pyroxenite and carbonated lherzolite. *Contributions to Mineralogy and Petrology*, *166*, 887–910. <https://doi.org/10.1007/s00410-013-0899-9>

- Grove, T. L., Elkins-Tanton, L. T., Parman, S. W., Chatterjee, N., Müntener, O., & Gaetani, G. A. (2003). Fractional crystallization and mantle-melting controls on calc-alkaline differentiation trends. *Contributions to Mineralogy and Petrology*, *145*, 515–533. <https://doi.org/10.1007/s00410-003-0448-z>
- Hammer, J., Jacob, S., Welsch, B., Hellebrand, E., & Sinton, J. (2016). Clinopyroxene in postshield Haleakala ankaramite: 1. Efficacy of thermobarometry. *Contributions to Mineralogy and Petrology*, *171*(7). <https://doi.org/10.1007/s00410-015-1212-x>
- Hammouda, T. (2003). High pressure melting of carbonated eclogites and experimental constraints on carbon recycling and storage in the mantle. *Earth and Planetary Science Letters*, *214*, 357–368. [https://doi.org/10.1016/S0012-821X\(03\)00361-3](https://doi.org/10.1016/S0012-821X(03)00361-3)
- Hartley, M. E., MacLennan, J., Edmonds, M., & Thordarson, T. (2014). Reconstructing the deep CO₂ degassing behaviour of large basaltic fissure eruptions. *Earth and Planetary Science Letters*, *393*, 120–131. <https://doi.org/10.1016/j.epsl.2014.02.031>
- Helz, R. T., & Thornber, C. R. (1987). Geothermometry of Kilauea Iki lava lake, Hawaii. *Bulletin of Volcanology*, *49*, 651–668. <https://doi.org/10.1007/BF01080357>
- Hirose, K., & Fei, Y. (2002). Subsolidus and melting phase relations of basaltic composition in the uppermost lower mantle. *Geochimica et Cosmochimica Acta*, *66*, 2099–2108. [https://doi.org/10.1016/S0016-7037\(02\)00847-5](https://doi.org/10.1016/S0016-7037(02)00847-5)
- Hirschmann, M. M. (2006). Water, melting, and the deep earth H₂O cycle. *Annual Review of Earth and Planetary Sciences*, *34*, 629–653. <https://doi.org/10.1146/annurev.earth.34.031405.125211>
- Ho, K., Ge, W., Chen, J., You, C., Yang, H., & Zhang, Y. (2013). Late Cenozoic magmatic transitions in the central Great Xing'an Range, Northeast China: Geochemical and isotopic constraints on petrogenesis. *Chemical Geology*, *352*, 1–18. <https://doi.org/10.1016/j.chemgeo.2013.05.040>
- Huang, J., & Zhao, D. (2006). High-resolution mantle tomography of China and surrounding regions. *Journal of Geophysical Research*, *111*, B09305. <https://doi.org/10.1029/2005JB004066>
- Jolivet, L., Faccenna, C., Becker, T., Tesauro, M., Sternai, P., & Bouilhol, P. (2018). Mantle flow and deforming continents: From India-Asia convergence to Pacific subduction. *Tectonics*, *37*, 2887–2914. <https://doi.org/10.1029/2018TC005036>
- Karato, S. (2011). Water distribution across the mantle transition zone and its implications for global material circulation. *Earth and Planetary Science Letters*, *301*, 413–423. <https://doi.org/10.1016/j.epsl.2010.11.038>
- Kawakami, Y., Yamamoto, J., & Kagi, H. (2003). Micro-Raman densimeter for CO₂ inclusions in mantle-derived minerals. *Applied Spectroscopy*, *57*, 1334–1339. <https://doi.org/10.1366/000370203322554473>
- Keiding, J. K., & Sigmarsson, O. (2012). Geothermobarometry of the 2010 Eyjafjallajökull eruption: New constraints on Icelandic magma plumbing systems. *Journal of Geophysical Research*, *117*, B00C09. <https://doi.org/10.1029/2011JB008829>
- Kelbert, A., Schultz, A., & Egbert, G. (2009). Global electromagnetic induction constraints on transition-zone water content variations. *Nature*, *460*, 1003–1007. <https://doi.org/10.1038/nature08257>
- Kimura, J. I., Sakuyama, T., Miyazaki, T., Vaglarov, B. S., Fukao, Y., & Stern, R. J. (2018). Plume-stagnant slab-lithosphere interactions: Origin of the late Cenozoic intra-plate basalts on the East Eurasia margin. *Lithos* *300-301*, 227–249. <https://doi.org/10.1016/j.lithos.2017.12.003>
- Kiseeva, E. S., Litasov, K. D., Yaxley, G. M., Ohtani, E., & Kamansky, V. S. (2013). Melting and phase relations of carbonated eclogite at 9–21 GPa and the petrogenesis of alkali-rich melts in the deep mantle. *Journal of Petrology*, *54*, 1555–1583. <https://doi.org/10.1093/ptrology/egt023>
- Kogiso, T., Hirose, K., & Takahashi, E. (1998). Melting experiments on homogeneous mixtures of peridotite and basalt: Application to the genesis of ocean island basalts. *Earth and Planetary Science Letters*, *162*, 45–61. [https://doi.org/10.1016/S0012-821X\(98\)00156-3](https://doi.org/10.1016/S0012-821X(98)00156-3)
- Kogiso, T., & Hirschmann, M. M. (2006). Partial melting experiments of biminerally eclogite and the role of recycled mafic oceanic crust in the genesis of ocean island basalts. *Earth and Planetary Science Letters*, *249*, 188–199. <https://doi.org/10.1016/j.epsl.2006.07.016>
- Krawczynski, M. J., Grove, T. L., & Behrens, H. (2012). Amphibole stability in primitive arc magmas: Effects of temperature, H₂O content, and oxygen fugacity. *Contributions to Mineralogy and Petrology*, *164*, 317–339. <https://doi.org/10.1007/s00410-012-0740-x>
- Kuritani, T., Kimura, J.-I., Ohtani, E., Miyamoto, H., & Furuyama, K. (2013). Transition zone origin of potassic basalts from Wudalianchi volcano, northeast China. *Lithos*, *156-159*(1-12). <https://doi.org/10.1016/j.lithos.2012.10.010>
- Kuritani, T., Ohtani, E., & Kimura, J.-I. (2011). Intensive hydration of the mantle transition zone beneath China caused by ancient slab stagnation. *Nature Geoscience*, *4*, 713–716. <https://doi.org/10.1038/ngeo1250>
- Kuritani, T., Xia, Q.-K., Kimura, J.-I., Liu, J., Shimizu, K., Ushikubo, T., et al. (2019). Buoyant hydrous mantle plume from the mantle transition zone. *Scientific Reports*, *9*(6549). <https://doi.org/10.1038/s41598-019-43103-y>
- Le Maitre, R. W. (1976). The chemical variability of some common igneous rocks. *Journal of Petrology*, *17*, 589–637. <https://doi.org/10.1093/ptrology/17.4.589>
- Li, J., & Wang, J. (2002). Mantle redox state evolution in Eastern China and its implications. *Acta Geologica Sinica*, *76*, 238–248. <https://doi.org/10.1111/j.1755-6724.2002.tb00089.x>
- Lim, W. H., Chen, L., Liu, J., Wang, X., Zhong, Y., & Zeng, G. (2017). Discovery of Cenozoic high-magnesium andesite in the Greater Khingan Range, Northeast China. *Geological Journal of China Universities (Chinese with Abstract in English)*, *23*, 16–25.
- Liu, C., Masuda, A., & Xie, G. (1994). Major- and trace-element compositions of Cenozoic basalts in eastern China: Petrogenesis and mantle source. *Chemical Geology*, *114*, 19–42. [https://doi.org/10.1016/0009-2541\(94\)90039-6](https://doi.org/10.1016/0009-2541(94)90039-6)
- Liu, J., Xia, Q. K., Deloule, E., Chen, H., & Feng, M. (2015). Recycled oceanic crust and marine sediment in the source of alkali basalts in Shandong, eastern China: Evidence from magma water content and oxygen isotopes. *Journal of Geophysical Research: Solid Earth*, *120*, 8281–8303. <https://doi.org/10.1002/2015JB012476>
- Liu, J., Xia, Q. K., Deloule, E., Ingrin, J., Chen, H., & Feng, M. (2015). Water content and oxygen isotopic composition of alkali basalts from the Taihang Mountains, China: Recycled oceanic components in the mantle source. *Journal of Petrology*, *56*, 681–702. <https://doi.org/10.1093/ptrology/egv013>
- Liu, J. Q., Chen, L. H., Wang, X. J., Zhong, Y., Yu, X., Zeng, G., & Erdmann, S. (2017). The role of melt-rock interaction in the formation of Quaternary high-MgO potassic basalt from the Greater Khingan Range, Northeast China. *Journal of Geophysical Research: Solid Earth*, *122*, 262–280. <https://doi.org/10.1002/2016JB013605>
- Liu, J. Q., Chen, L. H., Zeng, G., Wang, X. J., Zhong, Y., & Yu, X. (2016). Lithospheric thickness controlled compositional variations in potassic basalts of Northeast China by melt-rock interactions. *Geophysical Research Letters*, *43*, 2582–2589. <https://doi.org/10.1002/2016GL068332>
- Liu, J.-Q., Chen, L.-H., Zhong, Y., Lim, W. H., & Wang, X. J. (2017). Petrological, K-Ar chronological and volcanic geological characteristics of Quaternary Xunke high-Mg# andesites from the Lesser Khingan Range. *Acta Petrologica Sinica (Chinese with Abstract in English)*, *33*, 31–40.

- Liu, X., Zhao, D., Li, S., & Wie, W. (2017). Age of the subducting Pacific slab beneath East Asia and its geodynamic implications. *Earth and Planetary Science Letters*, *464*, 166–174. <https://doi.org/10.1016/j.epsl.2017.02.024>
- Lowenstern, J. B. (1995). Application of silicate-melt inclusions to the study of magmatic volatiles. In: *Magmas, Fluids and Ore Deposits* (J. F. H. Thompson, ed.), 71–100.
- Mallik, A., & Dasgupta, R. (2014). Effect of variable CO₂ on eclogite-derived andesite and lherzolite reaction at 3 GPa - Implications for mantle source characteristics of alkalic ocean island basalts. *Geochemistry, Geophysics, Geosystems*, *15*, 1533–1557. <https://doi.org/10.1002/2014GC005251>
- Mallmann, G., O'Neill, H., & St, C. (2013). Calibration of an empirical thermometer and oxybarometer based on the partitioning of Sc, Y and V between olivine and silicate melt. *Journal of Petrology*, *54*, 933–949. <https://doi.org/10.1093/ptrology/egt001>
- Martel, C., Champallier, R., Prouteau, G., Pichavant, M., Arbaret, L., Balcone-Boissard, H., et al. (2013). Trachyte phase relations and implication for magma storage conditions in the Chaîne des Puys (French Massif Central). *Journal of Petrology*, *54*, 1071–1107. <https://doi.org/10.1093/ptrology/egt006>
- Moore, L. R., Gazel, E., Tuohy, R., Lloyd, A. S., Esposito, R., Steele-MacInnis, M., et al. (2015). Bubbles matter: An assessment of the contribution of vapor bubbles to melt inclusion volatile budgets. *American Mineralogist*, *100*, 806–823. <https://doi.org/10.2138/am-2015-5036>
- Morgan, D. J., & Jerram, D. A. (2006). On estimating crystal shape for crystal size distribution analysis. *Journal of Volcanology and Geothermal Research*, *154*, 1–7. <https://doi.org/10.1016/j.jvolgeores.2005.09.016>
- Moussallam, Y., Edmonds, M., Scaillet, B., Peters, N., Gennaro, E., Sides, I., & Oppenheimer, C. (2016). The impact of degassing on the oxidation state of basaltic magmas: A case study of Kilauea volcano. *Earth and Planetary Science Letters*, *450*, 317–325. <https://doi.org/10.1016/j.epsl.2016.06.031>
- Moussallam, Y., Oppenheimer, C., Scaillet, B., & Kyle, P. R. (2013). Experimental phase-equilibrium constraints on the phonolite magmatic system of Erebus Volcano, Antarctica. *Journal of Petrology*, *54*, 1285–1307. <https://doi.org/10.1093/ptrology/egt012>
- Nikolaev, G. S., Ariskin, A. A., Barmina, G. S., Nazarov, M. A., & Almeev, R. R. (2016). Test of the Ballhaus-Berry-Green Ol-Opx-Sp oxybarometer and calibration of a new equation for estimating the redox state of melts saturated with olivine and spinel. *Geochemistry International*, *54*, 301–320. <https://doi.org/10.1134/S0016702916040078>
- Oppenheimer, C., Moretti, R., Kyle, P. R., Eschenbacher, A., Lowenstern, J. B., Hervig, R. L., & Dunbar, N. W. (2011). Mantle to surface degassing of alkalic magmas at Erebus volcano, Antarctica. *Earth and Planetary Science Letters*, *306*, 261–271. <https://doi.org/10.1016/j.epsl.2011.04.005>
- Papale, P., Moretti, R., & Barbato, R. (2006). The compositional dependence of the saturation surface of H₂O+CO₂ fluids in silicate melts. *Chemical Geology*, *229*, 78–95. <https://doi.org/10.1016/j.chemgeo.2006.01.013>
- Pertermann, M., & Hirschmann, M. M. (2003). Anhydrous partial melting experiments on MORB-like eclogite: Phase relations, phase compositions and mineral/melt partitioning of major elements at 2–3 GPa. *Journal of Petrology*, *44*, 2173–2201. <https://doi.org/10.1093/ptrology/egg074>
- Pichavant, M., & Macdonald, R. (2007). Crystallization of primitive basaltic magmas at crustal pressures and genesis of the calc-alkaline igneous suite: Experimental evidence from St Vincent, Lesser Antilles arc. *Contributions to Mineralogy and Petrology*, *154*, 535–558. <https://doi.org/10.1007/s00410-007-0208-6>
- Pichavant, M., Martel, C., Bourdier, J.-L., & Scaillet, B. (2002). Physical conditions, structure and dynamics of a zoned magma chamber: Mount Pelée (Martinique, Lesser Antilles arc). *Journal of Geophysical Research*, *107*(B5). <https://doi.org/10.1029/2001JB000315>
- Putirka, K. D. (2008). Thermometers and barometers for volcanic systems. *Reviews in Mineralogy and Geochemistry*, *69*, 61–120. <https://doi.org/10.2138/rmg.2008.69.3>
- Roedder, E. (1979). Origin and significance of magmatic inclusions. *Bulletin de Mineralogie*, *102*, 467–510. <https://doi.org/10.3406/bulmi.1979.7299>
- Rosenthal, A., Hauri, E. H., & Hirschmann, M. M. (2015). Experimental determination of C, F, and H partitioning between mantle minerals and carbonated basalt, CO₂/Ba and CO₂/Nb systematics of partial melting, and the CO₂ contents of basaltic source regions. *Earth and Planetary Science Letters*, *412*, 77–87. <https://doi.org/10.1016/j.epsl.2014.11.044>
- Scaillet, B., & Evans, B. W. (1999). The 15 June 1991 eruption of Mount Pinatubo. I. Phase equilibria and pre-eruption P-T-fO₂-fH₂O conditions of the dacite magma. *Journal of Petrology*, *40*, 381–411. <https://doi.org/10.1093/ptrology/40.3.381>
- Smart, K. A., Heaman, L. M., Chacko, T., Simonetti, A., Kopylova, M., Mah, D., & Daniels, D. (2009). The origin of high-MgO diamond eclogites from the Jericho Kimberlite, Canada. *Earth and Planetary Science Letters*, *284*, 527–537. <https://doi.org/10.1016/j.epsl.2009.05.020>
- Spandler, C., Yaxley, G., Green, D. H., & Rosenthal, A. (2008). Phase relations and melting of anhydrous K-bearing eclogite from 1200 to 1600°C and 3 to 5 GPa. *Journal of Petrology*, *49*, 771–795. <http://doi.org/10.1093/ptrology/egm039>
- Spandler, C., Yaxley, G., Green, D. H., & Scott, D. (2010). Experimental phase and melting relations of metapelite in the upper mantle: Implications for the petrogenesis of intraplate magmas. *Contributions to Mineralogy and Petrology*, *160*, 569–589. <https://doi.org/10.1007/s00410-010-0494-2>
- Steele-MacInnis, M., Esposito, R., Moore, L., & Hartley, M. E. (2017). Heterogeneously entrapped, vapor-rich melt inclusions record pre-eruptive magmatic volatile contents. *Contributions to Mineralogy and Petrology*, *172*(18). <https://doi.org/10.1007/s00410-017-1343-3>
- Tang, Y., Obayashi, M., Niu, F., Grand, S. P., Chen, Y. J., Kawakatsu, H., et al. (2014). Changbaishan volcanism in northeast China linked to subduction-induced mantle upwelling. *Nature Geoscience*, *7*, 470–475. <https://doi.org/10.1038/ngeo2166>
- Tauzin, B., Kim, S., & Kennett, B. L. N. (2017). Pervasive seismic low-velocity zones within stagnant plates in the mantle transition zone: Thermal or compositional origin? *Earth and Planetary Science Letters*, *477*, 1–13. <https://doi.org/10.1016/j.epsl.2017.08.006>
- Tollan, P., & Hermann, J. (2019). Arc magmas oxidized by water dissociation and hydrogen incorporation in orthopyroxene. *Nature Geoscience*, *12*, 667–671. <https://doi.org/10.1038/s41561-019-0411-x>
- Wallace, P. J. (2005). Volatiles in subduction zone magmas: Concentrations and fluxes based on melt inclusion and volcanic gas data. *Journal of Volcanology and Geothermal Research*, *140*, 217–240. <https://doi.org/10.1016/j.jvolgeores.2004.07.023>
- Wang, X.-J., Chen, L.-H., Hofmann, A. W., Mao, F.-G., Liu, J.-Q., Zhong, Y., et al. (2017). Mantle transition zone-derived EM1 component beneath NE China: Geochemical evidence from Cenozoic potassic basalts. *Earth and Planetary Science Letters*, *465*, 16–28. <https://doi.org/10.1016/j.epsl.2017.02.028>
- Waters, L. E., & Lange, R. A. (2015). An updated calibration of the plagioclase-liquid hygrometer-thermometer applicable to basalts through rhyolites. *American Mineralogist*, *100*, 2172–2184. <https://doi.org/10.2138/am-2015-5232>
- Wei, W., Hammond, J. O. S., Zhao, D., Xu, J., Liu, Q., & Gu, Y. (2019). Seismic evidence for a mantle transition zone origin of the Wudalianchi and Halaha volcanoes in northeast China. *Geochemistry, Geophysics, Geosystems*, *20*, 398–416. <https://doi.org/10.1029/2018GC007663>

- Whitney, D. L., & Evans, B. W. (2010). Abbreviations for names of rock-forming minerals. *American Mineralogist*, *95*, 185–187. <https://doi.org/10.2138/am.2010.3371>
- Widiyantoro, S., Ramdhan, M., Métaxian, J.-P., Cummins, P. R., Martel, C., Erdmann, S., et al. (2018). Seismic imaging and petrology explain highly explosive eruptions of Merapi Volcano, Indonesia. *Scientific Reports*, *8*(13656). <https://doi.org/10.1038/s41598-018-31293-w>
- Wojdyr, M. (2010). Fityk: A general-purpose peak fitting program. *Journal of Applied Crystallography*, *43*, 1126–1128. <https://doi.org/10.1107/S0021889810030499>
- Xia, Q. K., Liu, J., Kovács, I., Hao, Y. T., Li, P., Yang, X. Z., et al. (2017). Water in the upper mantle and deep crust of eastern China: Concentration, distribution and implications. *National Science Review*, *6*, 125–144. <https://doi.org/10.1093/nsr/nwx016>
- Xu, Y., Li, H., Hong, L., Ma, L., Ma, Q., & Sun, M. (2018). Generation of Cenozoic intraplate basalts in the big mantle wedge under eastern Asia. *Science China Earth Sciences*, *61*, 869–886. <https://doi.org/10.1007/s11430-017-9192-y>
- Yasuda, A., Fujii, T., & Kurita, K. (1994). Melting phase relations of anhydrous mid-ocean ridge basalt from 3 to 20 GPa: Implications for the behavior of subducted oceanic crust in the mantle. *Journal of Geophysical Research*, *99*, 9401–9414. <https://doi.org/10.1029/93JB03205>
- Yaxley, G. M., & Brey, G. P. (2004). Phase relations of carbonate-bearing eclogite assemblages from 2.5 and 5.5 GPa: Implications for petrogenesis of carbonatites. *Contributions to Mineralogy and Petrology*, *146*, 606–619. <https://doi.org/10.1007/s00410-003-0517-3>
- Zhang, L.-Y., Prelević, D., Li, N., Mertz-Kraus, R., & Buhre, S. (2016). Variation of olivine composition in the volcanic rocks in the Songliao basin, NE China: Lithosphere control on the origin of the K-rich intraplate mafic lavas. *Lithos*, *262*, 153–168. <https://doi.org/10.1016/j.lithos.2016.06.028>
- Zhao, D. (2004). Global tomographic images of mantle plumes and subducting slabs: Insight into deep Earth dynamics. *Physics of the Earth and Planetary Interiors*, *146*, 3–34. <https://doi.org/10.1016/j.pepi.2003.07.032>
- Zhao, Y.-W., Li, N., Fan, Q.-C., Zou, H., & Xu, Y.-G. (2014). Two episodes of volcanism in the Wudalianchi volcanic belt, NE China: Evidence for tectonic controls on volcanic activities. *Journal of Volcanology and Geothermal Research*, *285*, 170–179. <https://doi.org/10.1016/j.jvolgeores.2014.08.016>
- Zou, H., Fan, Q., & Yao, Y. (2008). U-Th systematics of dispersed young volcanoes in NE China: Asthenosphere upwelling caused by piling up and upward thickening of stagnant Pacific slab. *Chemical Geology*, *255*, 134–142. <https://doi.org/10.1016/j.chemgeo.2008.06.022>

References From the Supporting Information

- Baker, D. R., & Alletti, M. (2012). Fluid saturation and volatile partitioning between melts and hydrous fluids in crustal magmatic systems: The contribution of experimental measurements and solubility models. *Earth-Science Reviews*, *114*, 298–324. <https://doi.org/10.1016/j.earscirev.2012.06.005>
- Frezzotti, M. L., Tecce, F., & Casagli, A. (2012). Raman spectroscopy for fluid inclusion analysis. *Journal of Geochemical Exploration*, *112*, 1–20. <https://doi.org/10.1016/j.gexplo.2011.09.009>
- Gavrilenko, M., Herzberg, C., Vidito, C., Carr, M. J., Tenner, T., & Ozerov, A. (2016). A calcium-in-olivine geohygrometer and its application to subduction zone magmatism. *Journal of Petrology*, *57*, 1811–1831. <https://doi.org/10.1093/petrology/egw062>
- Newman, S., & Lowenstern, J. B. (2002). VolatileCalc: A silicate-melt-H₂O-CO₂ solution model written in Visual Basic for Excel. *Computers and Geosciences*, *28*, 597–604. [https://doi.org/10.1016/S0098-3004\(01\)00081-4](https://doi.org/10.1016/S0098-3004(01)00081-4)
- Wang, X., Chou, I. M., Hu, W., Burruss, R. C., Sun, C., & Song, Y. (2011). Raman spectroscopic measurements of CO₂ density: Experimental calibration with high-pressure optical cell (HPOC) and fused silica capillary capsule (FSCC) with application to fluid inclusion observations. *Geochimica et Cosmochimica Acta*, *75*, 4080–4093. <https://doi.org/10.1016/j.gca.2011.04.028>